Do imaging techniques add real value to the development of better post-Li-ion batteries?

Joanna Conder, Cyril Marino, Petr Novák, Claire Villevieille

Journal of Materials Chemistry A

REVIEW

Do imaging techniques add real value to the development of better post-Li-ion batteries?

Received 00th January 20xx,
Accepted 00th January 20xx

DOI: 10.1039/x0xx00000x

www.rsc.org/

Joanna Conder,[a,b,+] Cyril Marino,[a,+] Petr Novák[a,*] and Claire Villevieille[a,+,*]

Imaging techniques are increasingly used to study Li-ion batteries and, in particular, post-Li-ion batteries such as Li–S batteries, Na-ion batteries, and all-solid-state batteries. Results that appear impressive owing good image design and reconstruction are frequently published in high-impact-factor journals; however, questions have arisen about the added value of such results and the information they reveal about reaction mechanisms occurring in batteries during operation and/or degradation. We present here a review of imaging techniques and the knowledge acquired from these techniques for three systems: Li–S batteries, Na-ion batteries, and all-solid-state batteries. There are always advantages and disadvantages associated with these techniques, but beam damage remains the bottleneck to characterization. This factor needs to be considered seriously in order to obtain valuable outcomes that will enable improvements of battery performance and lifetime.

1. Introduction

Since the commercialization of Li-ion batteries by Sony in 1991,[1] researchers have aimed at increasing the specific energies of both negative and positive electrode materials by replacing graphite and $LiCoO_2$, respectively.[2] For negative electrodes, research is currently focused on alloy/conversion materials such as tin,[3] antimony,[4] phosphorus,[5] and silicon,[6] which exhibit outstanding specific charge compared with graphite. Although their specific charges are highly attractive, these materials participate in reactions that lead to increases in volume of roughly 200% during cycling, resulting in mechanical strain.[7] For positive electrodes, the aim is to increase the average electrochemical potential from 4 to 5 V vs. Li^+/Li, and thus increase the specific energy of Li-ion batteries.[8] To date, only two materials can fulfil these criteria. High-energy lithium-rich layered $Li_{1+x}(Ni,Mn,Co)O_2$ (NMC), a representative next-generation 5 V cathode material for Li-ion batteries, is able to cycle up to 4.5 V *vs*. Li^+/Li with a very high specific charge of more than 220 $mAh \cdot g^{-1}$.[9-12] However, this material suffers from some structural reorganization during cycling, leading to i) voltage fading and ii) transition metal leaching.[13-17] Eventually, both phenomena contribute to energy fading, limiting commercialization of NMC as a 5 V cathode for Li-ion batteries. As another example material, $LiNi_{0.5}Mn_{1.5}O_4$ (LNMO) spinel has a high operating voltage (~4.7 V *vs*. Li^+/Li) and offers an energy density of more than 600 $Wh \cdot kg^{-1}$ *vs*. Li^+/Li,[18-20] which is one of the highest values reported so far. Unfortunately, similar to the lithium rich NMC family, most of the redox reactions of LNMO materials take place in the region where the electrolyte is highly unstable, leading to rapid battery failure.[21-23] Despite all efforts to develop next-generation Li-ion batteries (based on 5 V cathodes), there are concerns about the viability of Li-ion batteries for the immense electric vehicle market in respect to the expected cost. Thus, over the last decade, new metal-based batteries (also called *post-Li* batteries) have been developed such as Li–S, Na-ion, solid-state batteries and Na-air (Figure 1).

Li–S batteries are considered the 'Holy Grail' of next-generation batteries and their commercialization is expected to be a breakthrough in terms of specific energy and cost. Unfortunately, the capacity of Li–S batteries decay quickly and the reversibility of the discharge/charge processes, often expressed as the coulombic efficiency, is low compared with this of commercial Li-ion batteries. The mechanism of capacity loss in Li–S cells is largely related to the mechanism of sulfur reduction to lithium sulfide (Li_2S) upon discharge (lithiation) and the development of the `polysulfides shuttle`[24].

[a] Paul Scherrer Institut, Electrochemistry Laboratory, CH-5232 Villigen PSI Switzerland. E-mail: petr.novak@psi.ch; claire.villevieille@psi.ch
[b] Current address: Institut de Science des Matériaux de Mulhouse, Carbon and Hybrid Material Group, 68100 Mulhouse, France
[+] These authors contributed equally to this work.

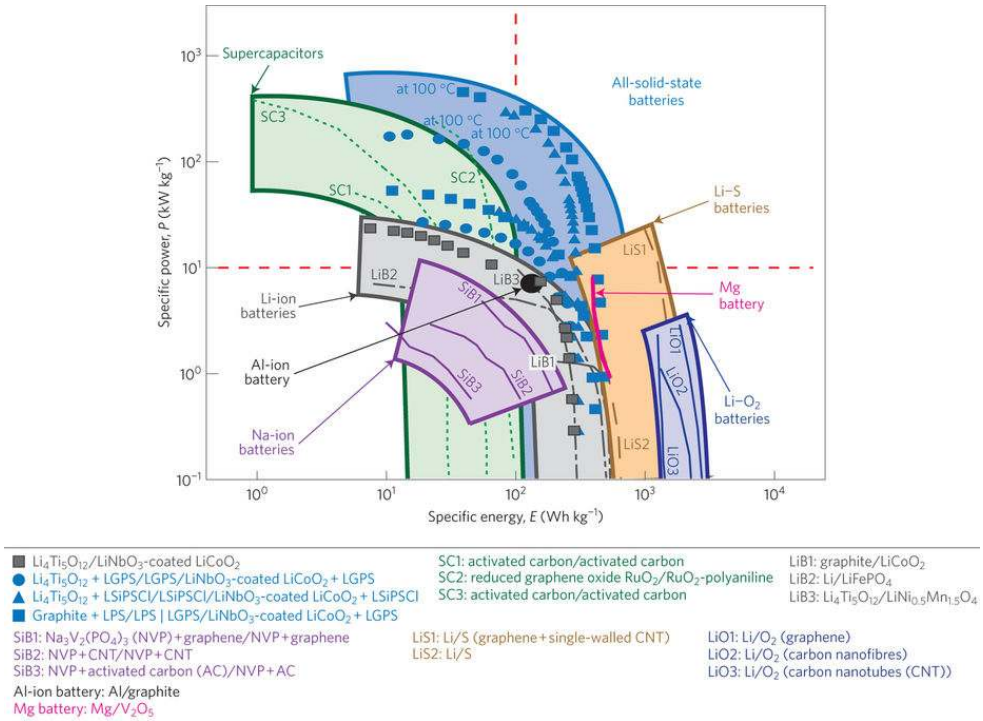

Figure 1 Ragone plots of cells discussed in this study and previously reported batteries and electrochemical capacitors. The red dashed lines indicate a specific energy of E = 100 Wh·kg^{-1} and a specific power of P = 10 kW·kg^{-1}. The devices powered by liquid electrolytes show an inverse relationship between specific energy and power. The all-solid-state cells simultaneously achieve at 100°C high energy and power (E > 100 Wh·kg^{-1} and P > 10 kW·kg^{-1}), which is difficult to achieve for conventional devices. Reproduced from Ref. [25] with permission from Nature Publishing Group.

Many solutions have been proposed and explored to address the 'polysulfide shuttle', for example, i) confinement of sulfur in either a conductive carbon matrix[26-34] or an ion-conducting polymer,[35-37] ii) integration of the metal oxides or sulphides electrocatalysts, iii) functionalization of the separator,[38-45] iv) introduction of a multifunctional interlayer,[46-48] and v) protection of Li metal through the use of electrolyte additives, *e.g.* $LiNO_3$[49] or the functionalization of the side of the separator facing the negative electrode.[50, 51]

Although these efforts have gradually moved Li–S battery chemistry closer to commercialization (Li–S battery prototypes developed by Sion Power[52] and Oxis Energy[53]), the existing challenges require further understanding of this complex battery chemistry at the interface, surface, bulk, and cell level.

The working principle of Na-ion batteries (NaB) is the same as that of Li-ion batteries. However, as demonstrated frequently in the literature, the know-how acquired for Li-ion batteries cannot be transferred directly to Na-ion batteries, and thus, systematic studies need to be undertaken on the positive and negative electrodes, including interactions at the interface between the liquid and the solid (solid electrolyte interphase (SEI), etc.).[54] Different families of materials, mostly derived from Li-ion chemistry, have been investigated. With the exception of $Na_{1.5}VPO_{4.8}F_{0.7}$, which shows a reversible specific charge of 100 mAh·g^{-1} at an average potential of 3.8 V vs. Na^+/Na,[55] other compounds based on polyanions,[56] Prussian blue analogues,[57] and organic cathodes[58] suffer from either limited working potentials (<3 V) or low specific charges (<90 mAh·g^{-1}). Layered oxide Na_xMO_2 (M = mixture of transition metals) compounds[59] fulfil the criteria of 'high' energy density[60] and, if paired with hard carbon as a negative electrode, deliver a specific energy of around 185 Wh·kg^{-1}.[61] For negative electrodes, two main categories of materials have been explored: insertion materials and conversion/alloying materials.[62] The former category relies mainly on carbonaceous materials (non-graphitic carbon materials or hard carbons able to deliver specific charges of 250–350 mAh·g^{-1})[63,64] and titanium-based oxides, which are less attractive owing to their lower energy storage abilities.[65] The latter category consists of conversion/alloying electrode materials, such as intermetallics (*e.g.* SnSb and $CuSbS_2$)[66,67-70] and metals (*e.g.* Sn and Sb),[71,72] all of which can achieve higher specific charges (>500 mAh·g^{-1}), similar to those in Li-ion batteries. However, these materials suffer from significant volume changes upon cycling, resulting in poor long-term stability. Finally, although the specific energies of Na-ion batteries are lower than those of their Li-ion counterparts, this post-Li technology will be most probably used as a complementary storage solution in the near future.

Beyond the "classical" electrochemical systems, Na metal was recently suggested for the application in Na-air battery[73], where it could compete with the Li-air counterpart in terms of manufacturing cost and the charge/discharge reversibility.[74] Except of the significantly lower overpotentials, the Na-air system, however, faces a number of challenges similar to those of Li-air battery, which constantly impedes technological progress in this field. In addition, the energy density of 'today's' Na-air batteries is pretty low and offers only a half of the theoretical energy density of the Li-air battery. [75-78]

All-solid-state Li batteries are believed to be the second 'Holy Grail', in term of safety owing to the use of a non-flammable solid electrolyte in place of the liquid electrolyte. To date, two types of solid electrolytes have mainly been used, namely, sulfur-based and ceramic-based materials. Sulfur-based electrolytes have reasonable ionic conductivities at room temperature, but suffer from very narrow voltage operating windows (generally, ca.1 V) and high toxicity when in contact with air or moisture (resulting in the release of H_2S gas). In contrast, ceramic-based solid electrolytes are known to be 'stable' against air or moisture (carbonate species are formed, but no hazardous gas is released), but suffer from low ionic conductivities, which restrict their use at room temperature. The mechanical stability of the entire electrode–electrolyte stack with prolonged cycling also has to be addressed to determine the potential of solid-state batteries. In addition, the counter electrode should be chosen carefully as dendrites can propagate along grain boundaries.[79] Fractures could appear and propagate in a similar manner when the active material is subjected to stress during cycling.

These novel technologies and their electroactive materials exhibit mostly unknown reaction mechanisms during electrochemical cycling, and the investigation and understanding of these mechanisms require new tools to characterize the surface and bulk properties.[80, 81] Imaging techniques are among the most advanced techniques used so far to assess the state-of-health of electrodes and stacks visually and to acquire knowledge about their morphologies, chemical compositions, and crystal structures, as well as the interactions between different components. In this review, we address questions as to whether imaging techniques and 3D reconstructions, which are the end-products of most of these studies, are powerful tools that can help develop and improve batteries, as well as monitor and assess their electrochemical performance in real time. Thus, we present recent results obtained in three different systems (Li–S, Na-ion, and all-solid-state Li-ion batteries), with emphasis not only on the main findings, but also on the main limitations of the imaging technique chosen for each study.

2. *Ex situ*? *In situ*? *Operando*?

Understanding the reaction mechanisms of battery materials is never simple, as numerous challenges need to be addressed. Therefore, different techniques have been developed over the last decades to follow and elucidate these reaction mechanisms. In the recent literature, specific terminology is used, namely, i) *ex situ*, ii) *in situ*, and iii) *operando*. *Ex situ* measurements involve cycling a standard electrochemical cell, stopping it at the desired potential, and then extracting the electrode from the electrochemical cell for analysis using the desired technique. During *in situ* measurements, the materials are cycled in dedicated cells and, after stopping, measurements of the electrode are carried out inside the cell at open circuit voltage (OCV). Finally, *operando* measurements involve investigating cells by performing measurements via the chosen technique while the cell is cycling. The latter two methods provide the most useful information, which is directly related to changes within the components of the cell.

For *ex situ* measurements, there are several problems to take into account. i) When a cell is stopped at the desired potential, the system is in a metastable state, which may lead to 'relaxation' of the materials, that is, by the time the characterization is performed, metastable phases may have changed and may not adequately reflect what occurred during cycling and/or side reactions can continue. ii) The number of samples needed to study a full reaction mechanism is quite high and the reproducibility of samples is not always guaranteed, which makes it difficult to acquire reliable results. iii) Samples usually become air and moisture sensitive during cycling *versus* Li, leading to the risk of spontaneous redox reactions before or during subsequent characterization. For these reasons, *in situ* measurements are preferred, as they avoid air and moisture exposure as well as relaxation of the cycled materials. However, the development of reliable cells for *in situ* investigations is a considerable challenge owing to the necessary compromise between good electrochemistry during cycling and the inherent constraints of the apparatuses in which the cells are placed for further characterization.[82] However, both types of experiments (*ex situ* and *in situ*) are generally needed to fully understand the reaction mechanisms.

3. Advantages and drawbacks of imaging techniques

As always, besides the advantages there are also some drawbacks of using imaging techniques to study the complex battery systems. Both of them are listed below in Table 1, in which we focus on the most common techniques.

Technique	Pros	Cons
Optical microscopy [83]	• Easy to use, fast imaging technique (no need of sample preparation) • Allows for investigation of different type of materials – gas, liquid or solid samples, in any shape and geometry • Provides insight into the dynamics of changes	• Difficult to adapt for *operando* conditions (difficult to meet all of the cell design requirements) • Requires an optically transparent window • Limited resolution (hardly down to sub-µm range)
SEM	• Easy to use, fast imaging technique • Able to probe different conductive and non-conductive (=> sputtering) battery materials: electrodes, separators, and metallic lithium • Able to investigate the surface and the cross-sections • Provides versatile information about the sample (topology, chemical composition (SEM/EDX)) • Can be used for *post-mortem* analyses (requires a suitable transfer chamber)	• Limited to *ex situ* measurements • Operates in high vacuum, detrimental to volatile sample components • Inherent risk of beam damage • Not able to resolve nano-materials (resolution down to only few tens of nm) • Often provides inaccurate quantitative/qualitative analysis (especially for light elements, e.g. O, C, N)
STEM [84]	• Relatively easy to use, high resolution imaging (the STEM detector can be added to SEM or FIB/SEM systems) • Able to resolve nano-materials and thin coatings (quick nano-analysis) • Provides information about the elemental and chemical composition of the sample (microanalysis possible by means of EDX or EELS)	• Limited to *ex situ* measurements • Inherent risk of beam damage • Requires laborious sample preparation (“dilution” of the sample which may alter its chemical state) • Operates in high vacuum, detrimental to volatile samples • *Post-mortem* analysis is often difficult
TEM	• *Operando* experiments are possible but not very common • Able to probe different battery materials: electrodes, separators, and metallic lithium • Provides information about the local chemical composition of the sample (microanalysis by means of EELS) • Can be used for *post mortem* analyses (requires a transfer chamber)	• Usually requires dedicated operator • Difficult to adapt for *operando* measurements • Inherent risk of beam damage • Requires laborious sample preparation (“dilution” of the sample which may alter its chemical state) • Operates in high vacuum, detrimental to volatile samples
Micro X-ray tomography	• Can be adapted to *operando* measurements (very challenging) • Able to probe the entire cell stack • Enables 3D reconstruction of the material structure • Provides information about the chemical composition (density map) • Can be used for *post mortem* analysis (embedded samples)	• Available generally at the synchrotron • Difficult to adapt for *operando* measurements (difficult to meet all of the cell design requirements) • Inherent risk of beam absorption (dilution of electrode materials necessary due to the presence of dense elements) • Cycling conditions need to be adapted to acquisition time resolution • Has limited beam resolution (µm range)
Nano X-ray tomography	• Is able to resolve internal porosity and nano structures • Enables 3D reconstruction of the material structure • Possibility of chemical mapping (via density map) • Can be used for *post mortem* analysis (embedded samples)	• Available almost exclusively at the synchrotron • Very difficult if not impossible to adapt for *operando* measurements (difficult to meet all of the cell design requirements) • Inherent risk of beam absorption (dilution of electrode materials necessary due to the presence of dense elements) • Cycling conditions need to be adapted to acquisition time
FIB/SEM	• Fast high resolution imaging technique • Able to precise mill the sample and prepare it for other analyses (e.g. TEM) • Enables tomographic microanalysis of the sample • Can be used for *post mortem* analyses (requires a transfer chamber)	• Destructive, time-consuming analysis • Is laden with artefacts (e.g. Ga^+ implementation, redeposition of the sputtered material, surface amorphization) • Inherent risk of beam damage (especially for soft materials) • Limited to solid samples

Table 1. Advantages and drawbacks of most commonly used imaging techniques to probe battery materials

4. Li–S Batteries

In the case of Li–S batteries, the mechanism underlying the polysulfide shuttle formation is not well understood. In addition, fundamental studies of this phenomenon are further impeded mainly because it takes place in the liquid phase. Therefore, most *operando* techniques developed and optimized to study Li-ion batteries are not suitable for investigating Li–S chemistry, which does not operate via insertion or conversion mechanisms.

Owing to the complexity of reaction mechanisms based mostly on liquid–liquid equilibria, it may seem almost impossible to track the formation and evolution of polysulfides in real time and spatially resolve the various intermediate species. Indeed, most studies (*e.g.* X-ray diffraction (XRD) studies) have been performed *ex situ*,[85-88] resulting in uncertainty as to whether the observed phenomena are solely related to battery chemistry or are eventually artefacts resulting from relaxation of the electroactive materials. In addition, *ex situ* results often do not coincide well with *in situ* and *operando* results,[89-92] and cannot be combined into one picture to explain the cause of capacity fading in Li–S batteries.

4.1. Positive electrodes

For Li–S chemistry, the morphology of the positive electrode and its evolution during cycling, in particular, changes in the sulfur distribution within the electrode upon repetitive dissolution–precipitation, are important performance-defining parameters. Moreover, it seems that further progress towards commercially viable Li–S batteries is largely dependent on understanding the rearrangement of the positive electrode during cycling and on developing effective strategies for maintaining its structural integrity, especially at high cycling rates.[93] Many efforts have been dedicated to positive electrode engineering and, more specifically, to the confinement of sulfur in various porous carbon matrices. The aim of this approach is to enhance the redox reaction kinetics, especially of short-chain polysulfides, which are less soluble in the electrolyte, by creating a conductive network while simultaneously stabilizing the electrochemical reactions within the positive electrode.[94, 95] Among various vacuum-based microscopic techniques,[85, 86, 96-98] scanning electron microscopy coupled to X-ray energy dispersion spectroscopy (SEM/EDX) has been employed frequently to characterize the microstructure and discriminate the elemental composition of sulfur/carbon composites, which are often complex. However, this technique cannot be considered reliable owing to the volatility of sulfur and its migration and continuous redistribution under high vacuum and at elevated temperatures, leading to contamination of originally sulfur-free areas of the electrode and, thus, to misinterpretation of the results.[99] In the case of SEM/EDX, the electron beam induces local increases in temperature, the magnitude of which depends mainly on the voltage applied during the measurement. In addition to the acceleration voltage, beam heating depends on the ratio of the total surface area to the scanned area.[100] Thus, the higher the magnification, the smaller the spot size and the more concentrated the electron dose interacting with the sulfur particles, which leads to significant mass loss—a severe consequence of radiation damage.[101] Apart from beam heating and radiation damage, the sublimation of sulfur[102-104] is another factor restricting the use of vacuum-based microscopic techniques, in particular, transmission electron microscopy (TEM) to analyse the distribution of sulfur within composite electrodes.[105] Approximately one monolayer of sulfur atoms per second is sublimed under vacuum.[106] As a consequence, using TEM, it takes ~40 min for a sulfur particle of several microns in size to almost completely disappear, leaving behind a residue of 'super-sublimated' polymeric sulfur, which is relatively stable under high vacuum (Figure 2). [105]

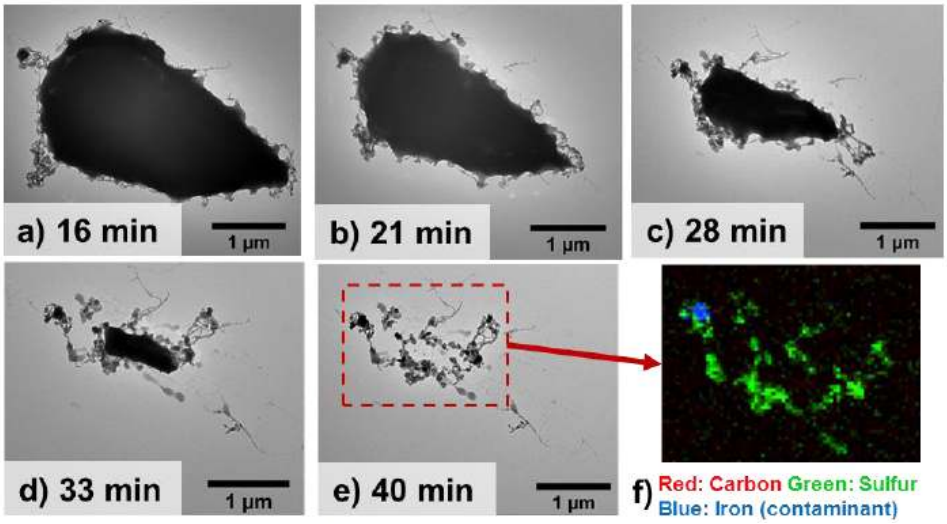

Figure 2 (a)–(e) Time series of sulfur particle sublimation in a FEI Tecnai F-20 TEM. The majority of the sulfur particle is sublimated by 40 min. Ambient temperature: 180 °C, ambient pressure: 8.8 × 10^{-8} Torr, beam dose: 10e^{-}·nm^{-2}·s^{-1}, exposure time per image: 2 s, sample not exposed to beam between images. (f) STEM EDX of the sulfur residue after

~3 h. The appearance of the residue is unchanged from that at 40 min. The residue was identified as a low-vapour-pressure sulfur polymer. Reproduced from Ref. [105] with permission from Cambridge University Press.

Encapsulating sulfur into a polymer, *e.g.* polyacrylonitrile[105] or polydopamine,[107] or into carbonaceous[96, 108] or other materials[109] may be a solution for sulfur sublimation by rendering this non-metal more stable for imaging under reduced pressure.[105, 110] Another possibility to reduce or even eliminate sublimation artefacts is to study sulfur-based electrode materials under either ambient or cryogenic conditions, away from the equilibrium vapour pressure of sulfur. Recently, Levin *et al.*[106] demonstrated the potential of non-conventional electron microscopes, such as air-SEM and cryo-TEM, to discriminate the distribution of sulfur in different carbon/sulfur composites (Figure 3).

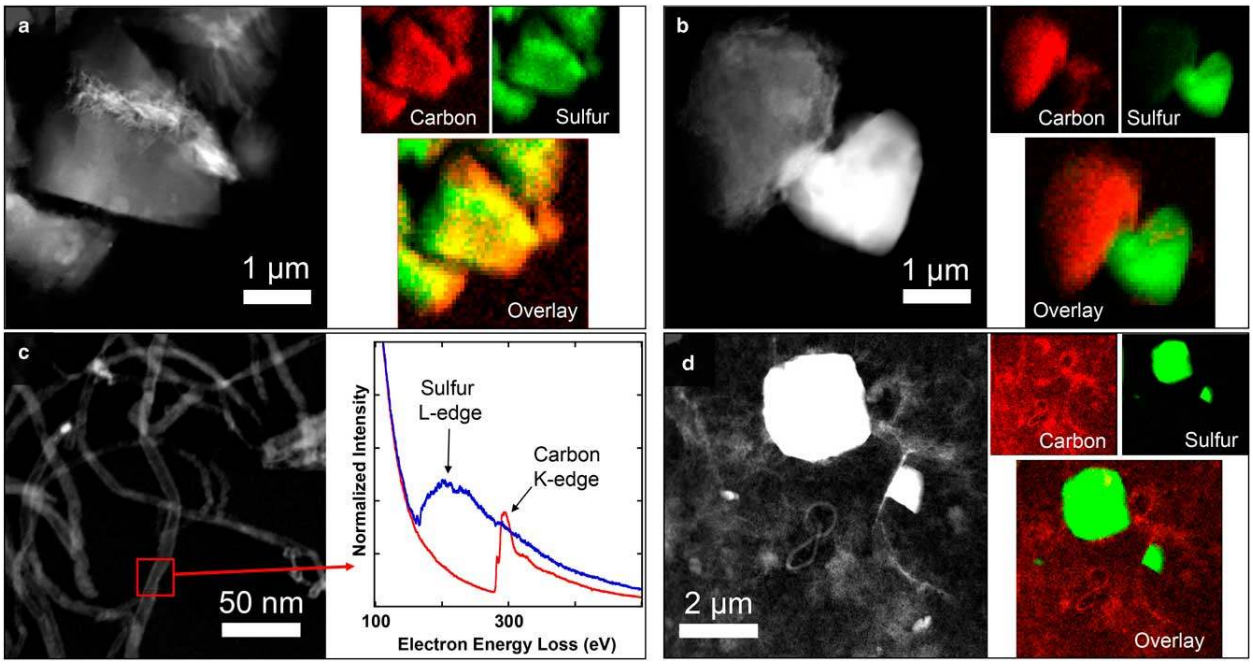

Figure 3 Cryo-scanning transmission electron microscope annular dark field (STEM ADF) images and X-ray energy dispersive spectroscopy (EDX) maps of (a) a composite of sulfur and activated gyroidal mesoporous and microporous carbon aG^{D}MC-15-10h, showing a high degree and homogeneity of sulfur infiltration (overlap in carbon and sulfur signals), and (b) a composite of sulfur and the same gyroidal mesoporous carbon G^{D}MC-15-1600°C without prior activation and very low microporosity, showing pure sulfur external to the carbon host, indicating poor infiltration efficiency. (c) Cryo-STEM image of carbon nanotubes after attempted sulfur melt infusion (tubes remain hollow). The electron energy loss spectroscopy (EELS) spectrum of the body of a tube (red) on a carbon support film shows little or no sulfur L-edge signal. The EELS spectrum of an elemental sulfur particle is shown for comparison (blue). (d) Cryo-STEM ADF image and EDX maps of a carbon nanotube sulfur composite (CNT-S), showing most sulfur external to the nanotubes. Reproduced from Ref. [106] with permission from Cambridge University Press.

The morphology of four different sulfur-infiltrated nanocomposite materials, namely, activated and non-activated ordered mesoporous carbons, carbon nanotubes, and mesoporous hollow carbon spheres, were studied below the sulfur sublimation point and at atmospheric pressure. The cryo-TEM and air-SEM results indicated that, for three out of four of the composites the majority of the active material was not infiltrated into carbon during melt infusion, forming sulfur particles of several microns in size outside the conductive network. Subsequent qualitative analysis of these composites by electron energy loss spectroscopy (EELS, Figure 3) and EDX revealed that the degree of sulfur infiltration into carbon is closely related to the physicochemical properties of the host material, in particular, the ratio of meso- and micropores and the total available surface area, both of which are important for enhancing the performance of Li–S cells.[111, 112] This conclusion could not have been reached by observation of sulfur/carbon composites using conventional electron microscopy. Further efforts should be concentrated on investigating changes in electrode morphology as a function of the state of charge (SOC), so that high-energy-density optimized sulfur/carbon composites can be produced and characterized with relative ease. However, to maximize the potential of microscopic techniques and be able to link the electrochemical performance to changes occurring within the electrodes in real time, either special *in situ/operando* cells have to be designed or sample holders have to be incorporated into already existing test cells. In this way, the lag time between cell disassembly and beginning imaging measurements can be minimized to allow metastable polysulfide intermediates to be captured.

Although the problems of sulfur sublimation and its continuous redistribution under reduced pressure are overcome by employing electron microscopes operated under

either cryogenic or ambient conditions, these two-dimensional (2D) characterization techniques fail to reveal spatial microstructural variations in the inherently three-dimensional (3D) sulfur-based electrodes.[113] In response to this, imaging techniques based on X-rays, *i.e.* transmission X-ray microscopy (X-ray TM), X-ray phase contrast tomography,[114] and X-ray radiography,[115, 116] have been explored as non-invasive high-resolution complex diagnostic tools to monitor the 'state-of-health' of batteries. Applied mostly in *operando* mode, these imaging techniques enable examination of the length and the breadth of an electrode to visualize microstructural changes occurring not only at or near its surface, but also across the thickness of the electrode, while the cell is cycling.[113] In addition, unlike their 2D counterparts, these techniques allow larger volumes to be probed, providing insights, with relatively high accuracy, into a number of parameters, such as the SOC-dependant particle size, the volume-specific surface area, and contact areas between the phases, which are difficult to quantify otherwise. Although the electrochemical performance of most tomography cells is often sacrificed to achieve high signal-to-noise ratios, low attenuation coefficients for components other than the material(s) of interest, and many other factors,[117] important conclusions can be still drawn from these microstructural studies. Yermukhambetova *et al.*[113] observed that upon cycling of a Li–S cell, the sulfur particle size increases, whereas the average volume-specific surface area decreases, suggesting progressive agglomeration of the active material (Figure 4). They also confirmed that once dissolved in the electrolyte and having undergone a chain of reduction reactions, the positive electrode loses its integrity.

Sulfur does not electrochemically precipitate at its original location but rather at any area with high electrical conductivity, preferably near the current collector. In addition, an attempt to further separate the contributions from the carbon, binder, and sulfur domains was made by increasing the spatial resolution through the use of *ex situ* nano-contrast tomography (CT). Despite the significantly smaller field of view (65 µm *versus* 750 µm) and the lower X-ray energies compared with those used for micro-CT, nano-CT has been shown to be a promising technique for *ex situ* imaging of single particles.

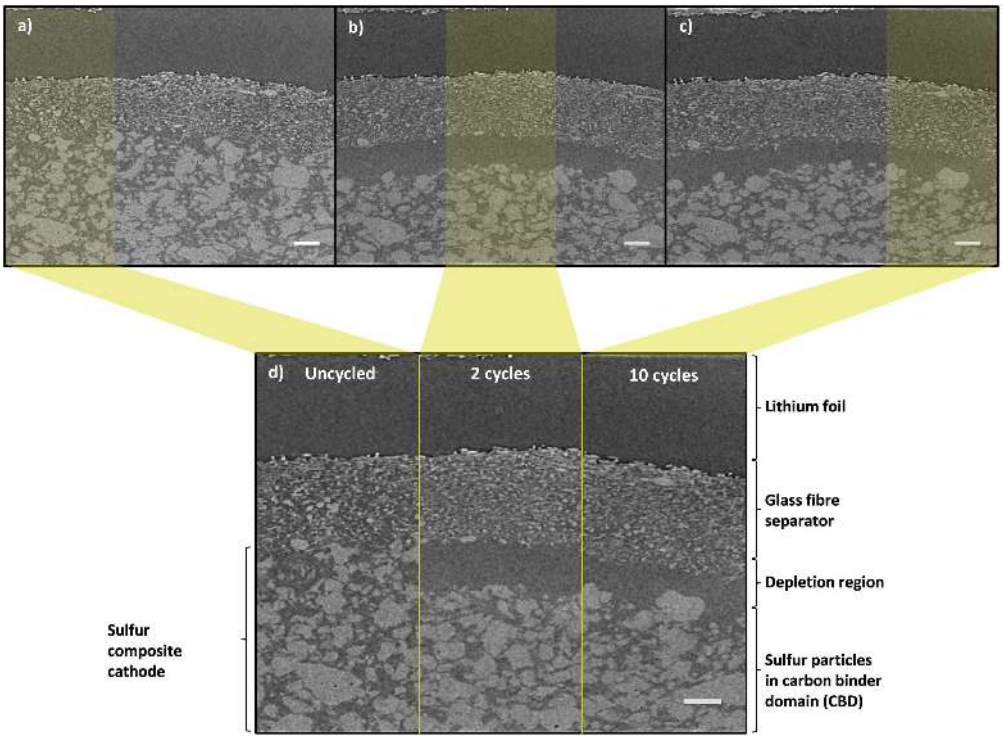

Figure 4 From top left (a–c) 2D virtual slices from tomography images of a Li–S cell before and after cycling for 2 and 10 cycles at 0.15 mA·cm^{-2}. (d) Combined image of the same virtual slice across different cycles. Scale bar is 50 µm. Reproduced from Ref. [113] with permission from Nature Publishing Group.

The sulfur and the carbon–binder domains can be also resolved while the cell is cycling, by 3D X-ray phase CT. This imaging technique was used by Zielke *et al.*[118] to investigate the morphology of a sulfur-based electrode coated on a 3D non-woven carbon (NwC) current collector upon ageing. Through careful segmentation and reconstruction of the electrode microstructure followed by meticulous data analysis, they demonstrated that the main changes in the positive electrode, that is, loss of the electrode integrity and significant redistribution of the active material, occur during the first cycle. After the first delithiation, sulfur migrates back into the top part of the 3D current collector and accumulates therein on further cycling (Figure 5). In addition, the particles become progressively smaller and disconnect from the conductive phase, thereby hindering high sulfur utilization and contributing to rapid specific charge decay.

Presumably, the decrease in sulfur particle size eventually leads to the formation of nano-sulfur, which is no longer observable by 3D X-ray phase CT because of the limitations of this technique for resolving sub-micron particles.[119] However, this X-ray based imaging technique provides further insights into the mechanism underlying the degradation of sulfur-based electrodes during cycling, which should serve as a guideline for improved positive electrode engineering. As a single characterization tool, the techniques mentioned thus far cannot be used to elucidate the reaction mechanism and resolve all of the questions associated with the complex electrochemical system of Li–S batteries. Thus, coupling two characterization techniques—one technique to probe morphological changes within the materials of interest as a function of the SOC and the other technique to follow the structural and chemical changes of the reacting species, as well as resolve them spatially—is a very attractive alternative. However, this multiscale characterization concept has been less frequently employed to study post-Li batteries than to study Li-ion batteries.[120-122]

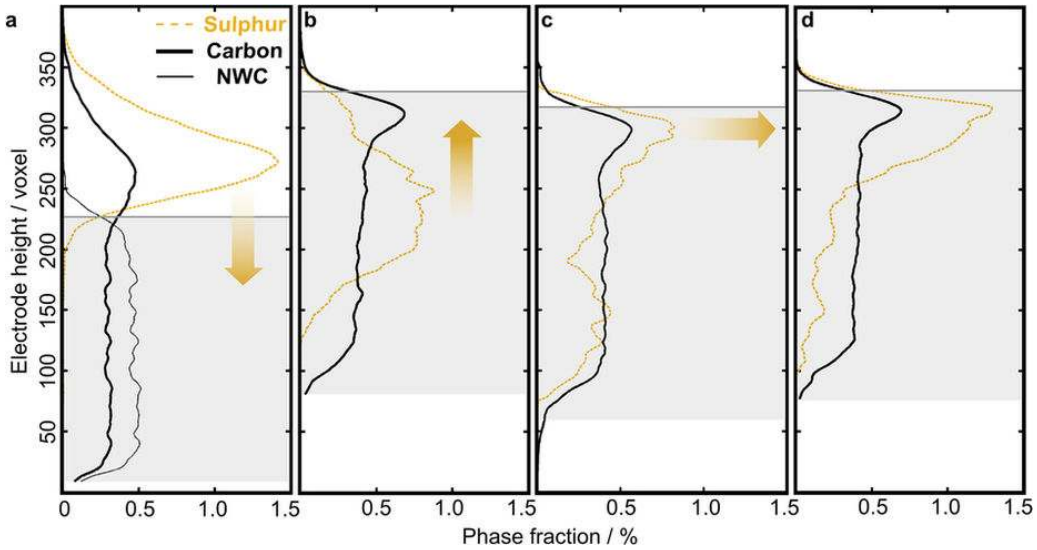

Figure 5 Through-plane height *versus* phase fraction of carbon and sulfur in reconstructed electrodes: (a) uncycled electrode, (b) after 1 cycle, (c) after 2 cycles, and (d) after 10 cycles. Reproduced from Ref. [118] with permission from Nature Publishing Group.

Nelson *et al.*[90, 123] combined XRD and X-ray TM to study the dependence of sulfur recrystallization during cell operation on positive electrode engineering. They compared super P–polyvinylidene fluoride (PVDF)-based electrodes containing as-received micrometre-sized sulfur either i) melted in conductive carbon, ii) mixed with carbon, or iii) obtained by reacting $Na_2S_2O_3$ with H_2SO_4, with sulfur particles coated with graphene-wrapped polyethylene glycol, prepared according to Wang *et al*.[124] They found that electrode engineering not only influences the morphology of the electrode, but also affects the recrystallization of sulfur during cycling.

Surprisingly, during *operando* measurements, the authors did not detect the formation of a crystalline lithium sulphide (Li_2S) phase, in contradiction to other *operando* studies.[125-127] This phase was only detected after letting the cell rest at the end of discharge, which causes doubt about the meaningfulness of the *operando* measurements (*e.g.* in respect to cell design and time resolution). This example also confirms that pouch cells are not the most reliable cell design for *operando* studies.[128] In the present case, the thermodynamic conditions are not met (mainly because of the lack of pressure in the cell) for detecting the Li_2S phase.

Recently Tonin *et al.*[119] used X-ray TM coupled to XRD to investigate the degradation phenomena occurring in Li–S cells, with a particular focus on determining the key parameters governing these processes. Not only did they observe that sulfur particles are always more concentrated at the top of the 3D carbon current collector (on which they were originally coated) and not in its depth, but also that the end-of-lithiation product (Li_2S) precipitates in a similar region and penetrates the 3D carbon current collector to a similar depth. In addition, they indicated that the incomplete reduction of S_8 to Li_2S along the lower-voltage plateau is one of the major factors limiting the performance of Li–S batteries.

Although the positive electrode is largely responsible for the capacity fading observed in Li–S cells, more than one component is required to assemble and operate such cells. In this respect, the use of Li metal as the negative electrode also has consequences.

4.2. Negative electrodes

Li metal is thermodynamically unstable upon contact with known organic electrolytes (typically developing a passivation layer) and tends to form Li electrodeposits of various morphologies (disordered dendritic or mossy-like structures[129]). These phenomena lead to side reactions, a significant resistance build-up, and the development of an overpotential during cycling, which contributes to the loss of coulombic efficiency and eventually causes cell failure. Several

strategies have been explored to tackle the limitations of this complex negative electrode and enable its safe use in Li–S and other Li metal batteries (LMBs). Most efforts have been dedicated to i) tuning the composition of the organic electrolyte in terms of solvent(s) and Li salt selection, as well as the addition of functional organic compounds,[130, 131] inorganic anions,[132] and halogenated salts;[133] ii) using non-liquid electrolytes instead of liquid electrolytes, *e.g.* single-ion conducting block copolymers;[134] or iii) tailoring the Li metal (*e.g.* graphene coating and ALD (atomic layer deposition) coating).[135-137] Although important advances have been made in recent years to mitigate the growth of Li dendrites and to enhance the coulombic efficiency of LMBs, most of the proposed strategies only prolong the dendrite initiation time and decrease the dendrite growth rate, and their function is often time-limited. In addition, existing solutions are often expensive and difficult to adapt to large-scale industrial production.[138] In this regard, further improvement and eventual successful commercialization of Li–S batteries and other LMBs might only be possible through smart engineering and harmonious adjustment of all the battery components based on a fundamental understanding of Li dendrite formation and growth. These dynamic, spatially localized processes can be studied by using advanced imaging techniques, for example, X-ray TM,[119] *operando* video microscopy,[139] and others.[140-143]

Using a multiscale approach, Tonin *et al.*[119] were able to track and visualize morphological changes not only within the positive electrode (sulfur electrode), but also within the counter electrode (metallic Li electrode; Figure 6). It is known that once the electrolyte comes into contact with Li metal, changes occur in the 'native' SEI layer.[144] The newly formed SEI, formed by organic and inorganic Li-based species,[145-147] acts as a shield against further decomposition of the organic electrolyte[148] and simultaneously as a multilayer bridge through which Li alternatingly dissolves (strips) and deposits (plates) during cycling. After the first discharge (lithiation of sulfur), nearly 16% of the Li thickness is consumed in a particular example and the Li electrode/electrolyte interface becomes highly inhomogeneous.[119] This value is ~5% higher than that calculated according to coulometry because the oxidation of Li is not uniform during cycling.

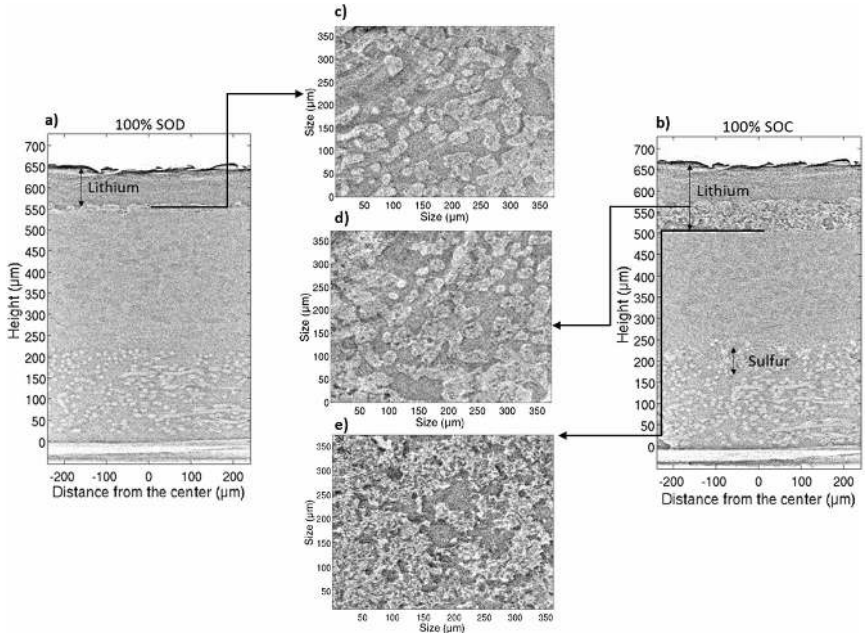

Figure 6 Vertical slices of the Li/S cell at the end of (a) the first discharge (100% SOD) and (b) the first charge (100% SOC). Horizontal slices of the cell at 100% SOD at heights of (a) 560 µm, (d) 570 µm, and (e) 505 µm. Reproduced from Ref. [119] with permission from Nature Publishing Group.

An inhomogeneous Li electrode/electrolyte interface triggers the formation of mossy Li, which forms a porous layer on the dense Li and hinders the recovery of its original morphology. Although mossy Li does not participate in any electrochemical reaction, it consumes Li ions and the electrolyte, resulting in a continuous decrease in cell performance and risks to safe operation.

Li metal stripping–plating is a very complex process, even without contributions from the other electrode, here, a sulfur-based electrode. Therefore, in many studies, this process has been decoupled from other electroactive materials and characterized separately in either a symmetric cell configuration[139-143, 146] or *versus* the deposition substrate, for example, stainless steel.[149] The latter configuration was used to study the reaction between metallic Li, polysulfides, and $LiNO_3$ as an electrolyte additive to directly observe Li dendrite formation using *in situ* optical microscopy. It has been shown that, by carefully adjusting the concentration of the polysulfide and $LiNO_3$, dendrite growth can be minimized and a stable and uniform SEI layer can be formed on the surface of Li, thereby contradicting the lack of synergy between these two electrolyte 'additives' (Figure 7).[149]

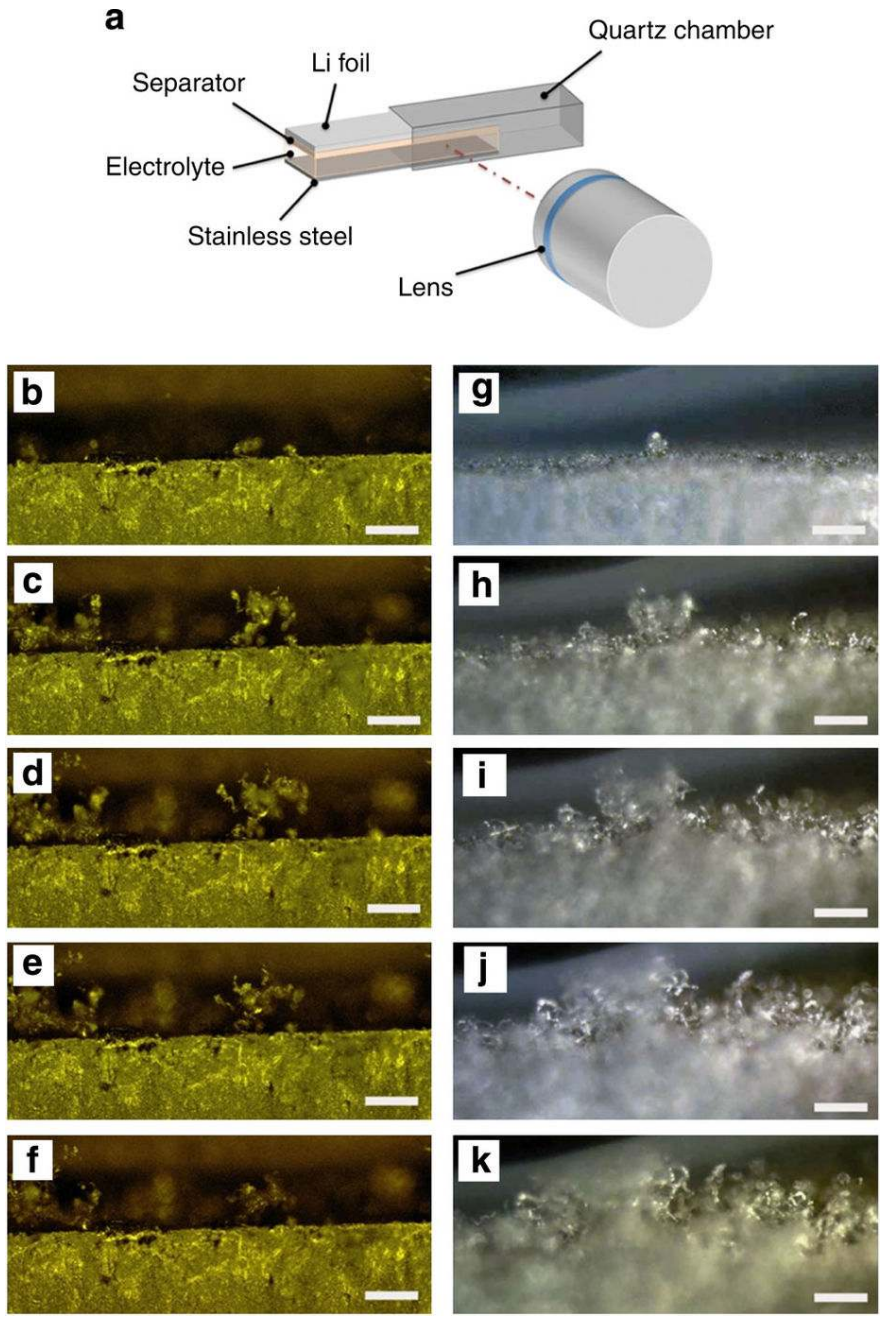

Figure 7 *In situ* optical microscopy study of Li dendrite formation. (a) Schematic illustration of a quartz cell device with transparent windows and a rectangular empty interior as the cell housing, in which a sandwich structure of Li metal, separator, and stainless steel substrate was assembled. The fabricated cell was put on the stage of an optical microscope with the transparent window facing the lens for *in situ* characterization. (b–f) A series of dark-field optical microscope images of the cell cross-section with increasing Li deposition time revealing the process of Li dendrite growth at 5 $mA \cdot cm^{-2}$ on the stainless steel substrate using an electrolyte with both Li_2S_8 and $LiNO_3$. (g–k) A series of dark-field optical microscope images of the cell cross-section with increasing Li deposition time showing the process of Li dendrite growth using an electrolyte with only $LiNO_3$ at the same current density as (b–f). Scale bar: 100 µm. Reproduced from Ref. [149] with permission from Nature Publishing Group.

4.3. Contributions from imaging techniques to the understanding of Li–S batteries

Although pairing a sulfur-based electrode with Li metal seems to be a simple and energy-density-effective solution for future battery applications, the lack of a deep understanding about the liquid/solid interactions of sulfur and its polysulfide intermediates with Li metal hampers the design of stable and safe operating Li–S batteries, and, thus, their rapid commercialization. To realize such an understanding, one should begin with simplified model cells before targeting the complex electrochemical mechanisms of real systems. Unfortunately, in the case of Li–S chemistry, the dynamics of polysulfide shuttle formation cannot be mimicked without a Li source in the cell. In this respect, imaging techniques can

provide important and invaluable insight into the battery processes, in particular, into the evolution of the positive electrode morphology. In addition, these techniques can be used to study one parameter at a time, *e.g.* the impact of the electrode formulation. Imaging of Li allows investigation of the consequences of using this highly reactive metal as an electrode, *e.g.* the non-uniform redeposition of Li during charging and the thermodynamic incompatibility of Li metal with the electrolyte.[144] Unfortunately, the undertaken methods (*i.e.* selection and combination of characterization techniques) are often too few and their spatial resolution is too low (*e.g. operando* video microscopy[139]) for observing dynamic nucleation and the initiation of Li dendrite growth on the nanometre scale.

5. Na-ion batteries

Because of the greater size/mass of Na relative to Li and its higher standard electrode potential (-2.71 V *vs*. -3.04 V vs. SHE), Na-ion batteries were hardly considered as a possible solution for storage applications.[150,] However, these facts are not especially relevant if Na is considered in its ionic form and not in its metallic form. In commercial full cells, where both anode and cathode are based on Na host materials, the energy density gap between Na and the Li systems is considerably reduces to only 30% instead of a factor of 3 (based on metal mass). For instance, $NaCoO_2$ has a theoretical specific charge of 235 $mAh{\cdot}g^{-1}$ with a cell voltage of around 3.5 V, whereas the theoretical specific charge of $LiCoO_2$ is 274 $mAh{\cdot}g^{-1}$ with a cell voltage of 4 V.[151] Current research on hard carbons as negative electrode materials has demonstrated reversible specific charges of 300 $mAh{\cdot}g^{-1}$,[152] which is not far from that of commercial graphite. Additionally, Na is one of the most abundant and cheap elements on earth,[153] and Al, which does not alloy with Na, can be used as a current collector in Na systems, leading to cost and mass reductions for the overall battery.

Unfortunately, the knowledge acquired with Li systems cannot be transferred directly to Na systems. For instance, the PVDF binder, commonly used in Li systems, is unstable at low potentials[154] and graphite, used as a reference anode material in LiB, hardly intercalates Na ions.[155] It is therefore important to investigate systematically the electrode materials, their interactions at the liquid/solid interface (electrolyte/electrode), and the overall cell.

Typical characterization methods, such as XRD,[156,157] X-ray absorption spectroscopy (XAS),[158,159,160] nuclear magnetic resonance (NMR),[161, 162] Raman spectroscopy,[163] and X-ray photoelectron spectroscopy (XPS),[154] have been successfully used to reveal the electrochemical mechanism of Na^+ reactions in electrode materials. Different electrochemical reaction pathways were found compared with those relevant in Li technology, confirming that knowledge cannot be transferred easily between systems. For instance, nine potential plateaus were detected in the sodiation curve of Na_xCoO_2 ($0.5 < x < 0.82$),[164] whereas only a sloping region was reported for $LiCoO_2$, and two potential plateaus were detected for Na_xFePO_4,[165] whereas only one was reported for $LiFePO_4$ in Li-ion batteries.

To date, most studies dedicated to investigating new materials for Na-ion batteries have focused on reaction pathways and targeting higher energies, but only a few have dealt with investigating the evolution of particle morphology/structure and the diffusion of Na^+ in the electrode material during the electrochemical process.

5.1. Imaging techniques on the material level

Imaging techniques such as SEM, FIB-SEM, and TEM are commonly used to extract local information about particle size/morphology and the impact on electrochemical performance.[166-167] While these techniques may be useful at the pristine stage to observe the shape of the materials (*e.g.* platelet-shaped structures,[168] flower-like structures,[169] and fibres[170]) and the internal porosity of particles,[113] they generally fail to provide reliable information of the evolution of the materials during cycling owing to changes in the materials chemistry (electrode extraction, washing, drying, etc. leads often to chemical modification) before investigation. Thus, it is commonly accepted that *in situ* and *operando* techniques are more suitable. During sodiation and desodiation processes, the materials typically undergo several transitions, leading to volume changes (a few percent for insertion-based materials and up to several hundred percent for conversion/alloying reactions). Imaging techniques have been used to follow this 'breathing' process of the materials, as well as the interaction of the materials with the other electrode components (*i.e.* binder and conductive carbon).

Examination of the sodiation of a carbon nanofibre (CNF) by *operando* TEM[171] showed that the inner fibre layer of crystalline carbon and the outer fibre layer of disordered carbon increased in volume by about 6% (Figure 8). Coupling these results with electrophoretic deposition, (EPD) measurements revealed that Na ions are inserted between the layers composing the fibres rather than within the graphitic layers. Additionally, several cracks were found along the fibres during the sodiation process. The authors assigned this phenomenon as contributing to electrochemical performance fading.

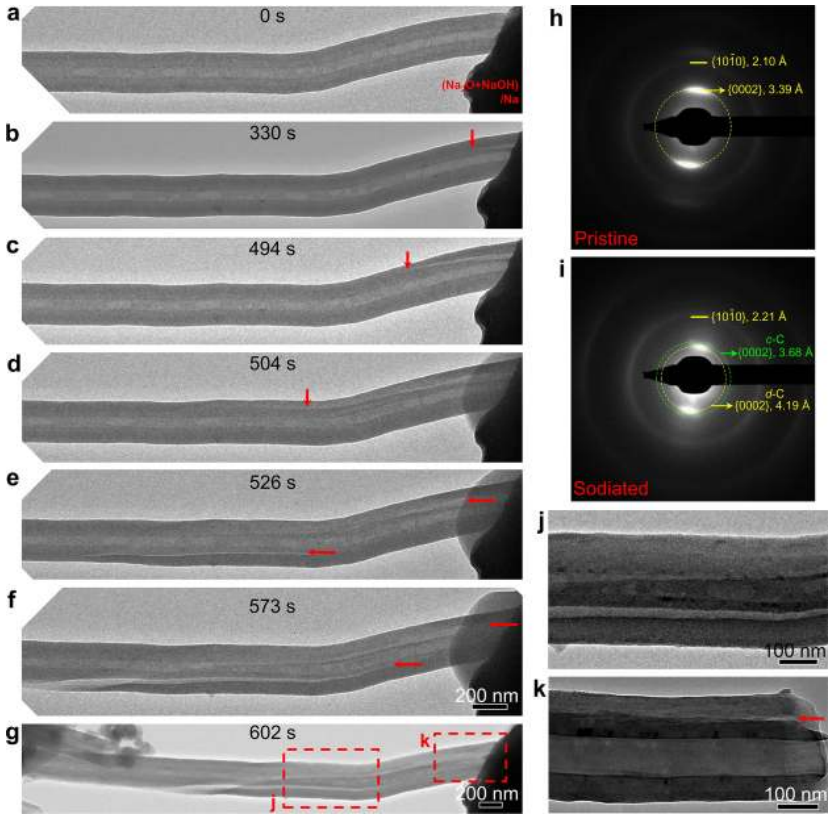

Figure 8 Sodiation-induced crack nucleation and propagation in a hollow bilayer carbon nanofibre (CNF). The experiment was conducted under beam-on conditions with very weak electron-beam exposure. (a) Pristine CNF. (b–g) Dynamic process of sodiation-induced crack nucleation and propagation. Upon sodiation, a crack is observed to nucleate from the contact point between the CNF and the Na_2O/Na electrolyte, and it extends from one end to the other end in the longitudinal direction. The red arrows indicate the crack and its propagation front. (h,i) EDPs of the CNF before and after the sodiation. (j,k) Magnified images showing the crack close to the c-C/d-C interface. Reprinted with permission from Ref. [171]. Copyright (2017) American Chemical Society.

Similarly, Seidl *et al*.[172] performed electrochemical scanning tunnelling microscopy (EC-STM) to investigate the co-intercalation process of Na ions into graphite in a glyme-based electrolyte. Using 3D topographic image reconstruction, they were able to evaluate the expansion of the graphite lattice upon cycling. They identified some intermediate metastable phases, such as NaC_{30}, but determined that this electrochemical reaction is dependent on the electrolyte solvent, *i.e.* glyme. Similar experiments have also been reported using less expensive technology consisting of only a CCD (charge-coupled devices) camera with a special set-up, where the Na co-intercalation process in highly ordered pyrolytic graphite (HOPG) was visually followed by the appearance of 'lines' along the graphite planes corresponding to the diffusion of Na ions (Figure 9).[173]

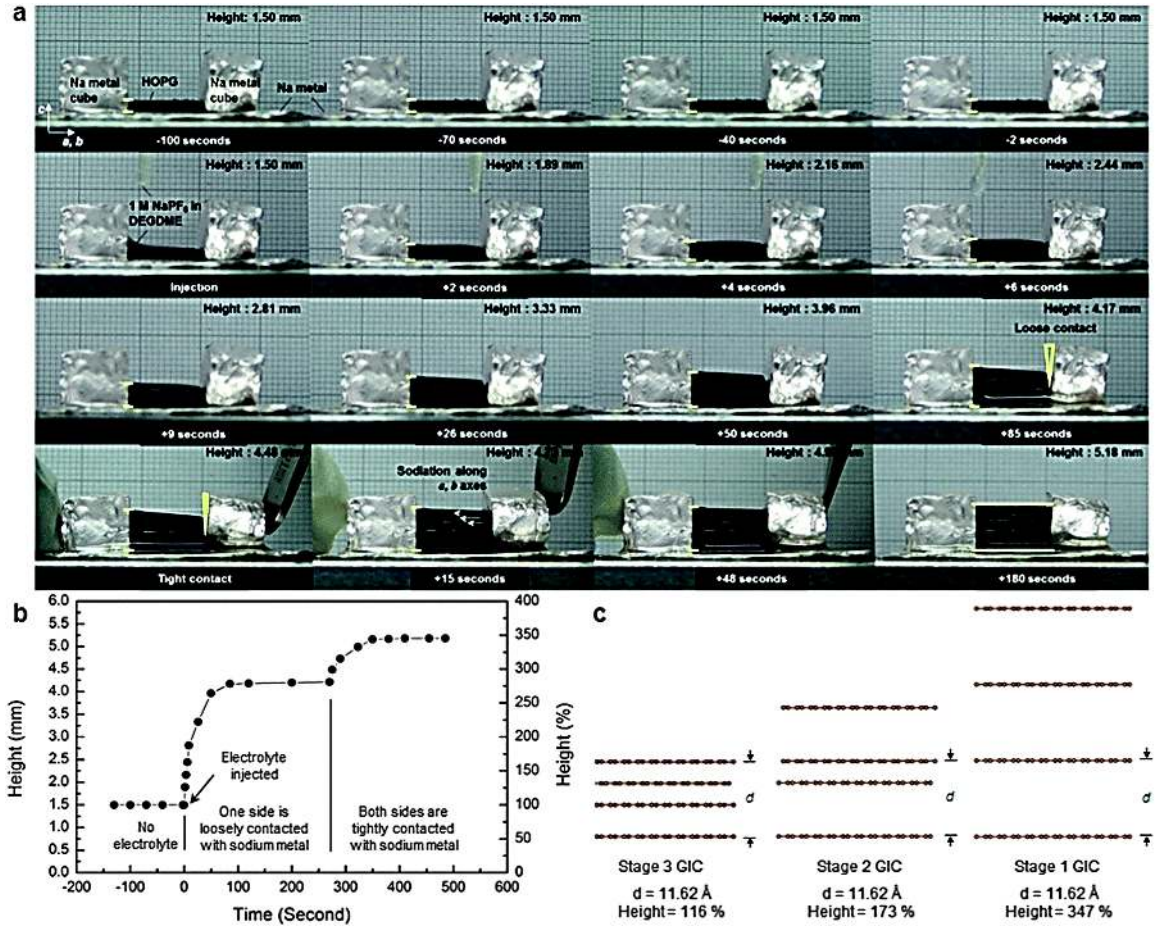

Figure 9 Expansion of highly ordered pyrolytic graphite (HOPG) along the c axis with chemical Na–ether intercalation. (a) Real-time snapshots of HOPG under direct contact with Na metal before and after exposure to 1 M $NaPF_6$ in DEGDME solution, (b) height of HOPG measured during the intercalation process, and (c) schematic comparison of the height and c lattice parameter of graphite for hypothetical stage 3 GIC, stage 2 GIC, and stage 1 GIC. Reproduced from Ref. [173] with permission from The Royal Society of Chemistry.

Other materials studied by microscopy techniques include spinel $Li_4Ti_5O_{12}$ (LTO) cycled *versus* Na. Sun *et al*.[174] performed an investigation using *ex situ* STEM at different SOC. They demonstrated that sodiation proceeded through three different phases: the unreacted LTO phase, the sodiated $Na_6LiTi_5O_{12}$ phase, and the fully lithiated $Li_7Ti_5O_{12}$ phase (once sodiation starts, Na ions are inserted into LTO, resulting in further reaction of the Li ions with LTO to form $Li_7Ti_5O_{12}$). Interestingly, this experiment allowed the deduction that the diffusion of Na ions into the material caused the displacement of Li ions.

For materials that react through conversion/alloying-based processes, imaging techniques are generally used to study important volume changes they occur during cycling. Imaging techniques have been employed to characterize the 'breathing' of electroactive materials and the mechanical stability of electrodes.

Operando hard X-ray nanotomography was used to investigate the sodiation/desodiation process in Sn spherical particles.[175] Upon sodiation, the spheres grew, as expected for an alloying reaction, and this expansion was followed by the appearance of several fractures on big agglomerates (>10 µm) at the end of sodiation (Figure 10). Similar observations were made by Villevieille *et al*. for the lithiation of Sb.[176] After the first sodiation, the morphology of Sn did not evolve as much during further cycles owing to the minor volume change recorded between the end of charge and the end of discharge. This result was supported by the electrochemical performance, which showed that Sn delivers a poor specific charge compared with the theoretical value. Interestingly, differences were found with the Li system. During delithiation, *i.e.* when Li ions are extracted from Li_xSn_y alloys, pulverization of the particles occurs, leading to severe capacity fading. Surprisingly, despite higher stress in the Na system than in the Li system, the electrochemical performance of the Na system is more favourable. Similar observations have been made for the Sb system, where the capacity during cycling was more stable for the Na ion system than for the Li ion system.[177] An *operando* TEM analysis performed on Sn particles coated with a thin layer of Al_2O_3[178] demonstrated that these core–shell particles buffer the volume change, resulting in better mechanical stability upon cycling, despite a visible volume change. *Operando* TEM measurements (using a solid electrolyte) were also used to follow the growth of particles upon sodiation in Sb thin films,[179] Sn spheres,[175] SnO_2 nanowires,[180] and Ge nanotubes.[181]

Journal of Materials Chemistry A

REVIEW

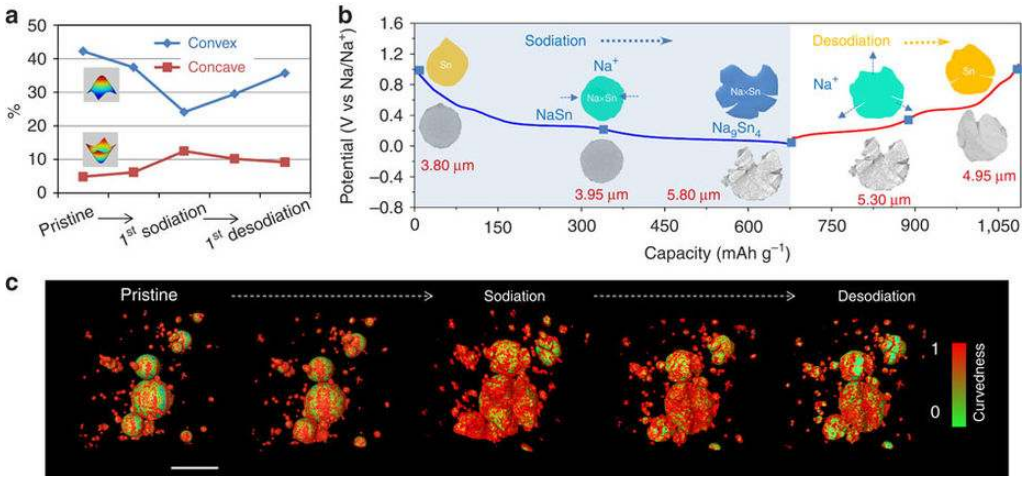

Figure 10 (a) Evolution of the two principal surface curvatures, convex and concave, during the first electrochemical cycle. (b) Schematic illustration (colour) showing surface curvature changes and the corresponding real cross-sectional images (grey) of selected particle. The discharge/charge profile is presented as the background. (c) 3D view of the evolution of surface curvedness during the first electrochemical cycle. The curvedness is calculated based features with the two principal curvatures, convex and concave. Reproduced from Ref. [175] with permission from Nature Publishing Group.

Additional studies on conversion-based materials have been conducted to elucidate sodiation/desodiation reaction mechanisms. Nie *et al.*[182] elucidated the electrochemical mechanism of Zn_4Sb_3 nanowires using a high-angle annular dark field (HAADF) detector coupled to an *operando* STEM/TEM investigation. Two phases were identified at the end of sodiation, $NaZn_{13}$ and NaZnSb. *Operando* TEM was found to be a suitable technique for observing fast Na diffusion into the nanowire, as contrast between sodiated and unsodiated phases was observed after only 12 s of cycling (Figure 11). Similar studies have been undertaken on SnS_2[183] where it was possible to follow Na diffusion into the material by *operando* TEM. This study also revealed the formation of an intermediate metastable phase, Na_xSnS_2, which was not detected in conventional XRD measurements because the collection time was too long. This technique was further applied to other systems (CuO,[184] Ni_3S_2,[185] and Co_9S_8[186]), as the metastable equilibria of conversion/alloy-based materials require *operando* techniques to detect new phases on the timescale of seconds. Moreover, XRD–CT was used to follow the sodiation of a phosphorus electrode at different SOC.[187] At the end of discharge, more Na_3P was found close to the separator than to the current collector. A relaxation effect was suggested by the authors to explain this phenomenon.

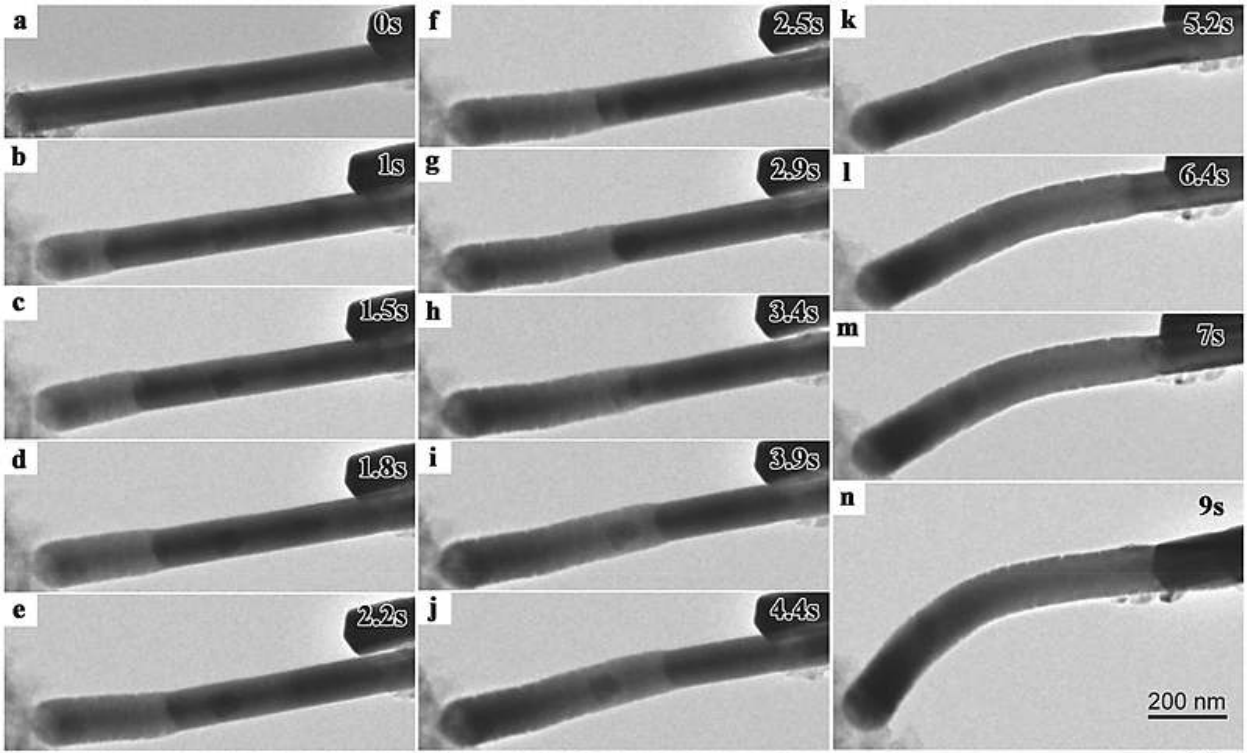

Figure 11 Ultrafast sodiation process for an individual Zn_4Sb_3 nanowire during charging at -1.0 V against Na metal coated with a NaOH/Na_2O layer. (a–n) Time-lapse morphology evolution of the Zn_4Sb_3 nanowire. The nanowire expanded in both the radial and axial directions after the reaction front passed by. Adapted from Ref. [182] with permission from John Wiley and Sons.

As previously mentioned, most of the imaging techniques employed so far are dedicated to the study of reaction mechanisms at the negative electrode. However, despite being less sensitive to structural changes, some cathode materials have also been investigated at different SOC. Xiang *et al*.[188] investigated the electrochemical mechanism of $NaFePO_4$ (NFP) with TEM. TEM images of the cycled material revealed the presence of an additional amorphous phase between the NFP and $FePO_4$ phases. This discovery was further confirmed by additional characterization techniques, such as XRD and pair distribution function (PDF), which suggested that NFP undergoes a tri-phase reaction mechanism that has not yet been detected. A combination of *operando* transmission X-ray microscopy (TXM) and X-ray absorption near edge structure (XANES) were chosen to study sodiation/desodiation mechanisms in layered oxide compounds. In the case of $NaNi_{1/3}Fe_{1/3}Mn_{1/3}O_2$,[189] X-ray TM images indicated that the surface morphology was unchanged after the first charge, but different chemistries were reached (Figure 12).

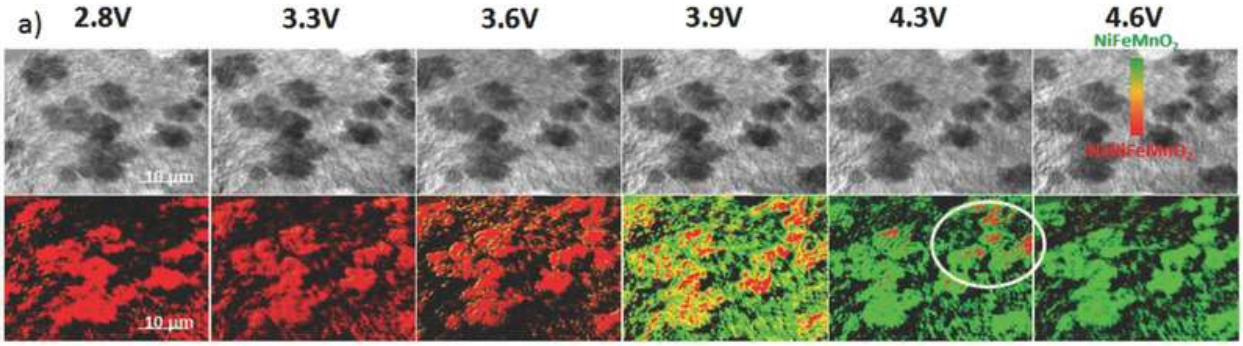

Figure 12 Morphology evolution and chemical phase mapping of $Na_{1-\delta}Ni_{1/3}Fe_{1/3}Mn_{1/3}O_2$ using *operando* TXM imaging during the desodiation reaction. Adapted from Ref. [189] with permission from John Wiley and Sons.

For the $NaNiO_2$ phase,[190] Wang *et al*. examined a single particle that did not evolve from the morphological point of view upon cycling, as shown in Figure 13. However, XANES mapping suggested that desodiation proceeded in two different ways: i) from the core of the particle and ii) from particles located at the bottom part of the electrode, *i.e.* close to the current collector, generating a double gradient in the particle and in the electrode.

Journal of Materials Chemistry A

REVIEW

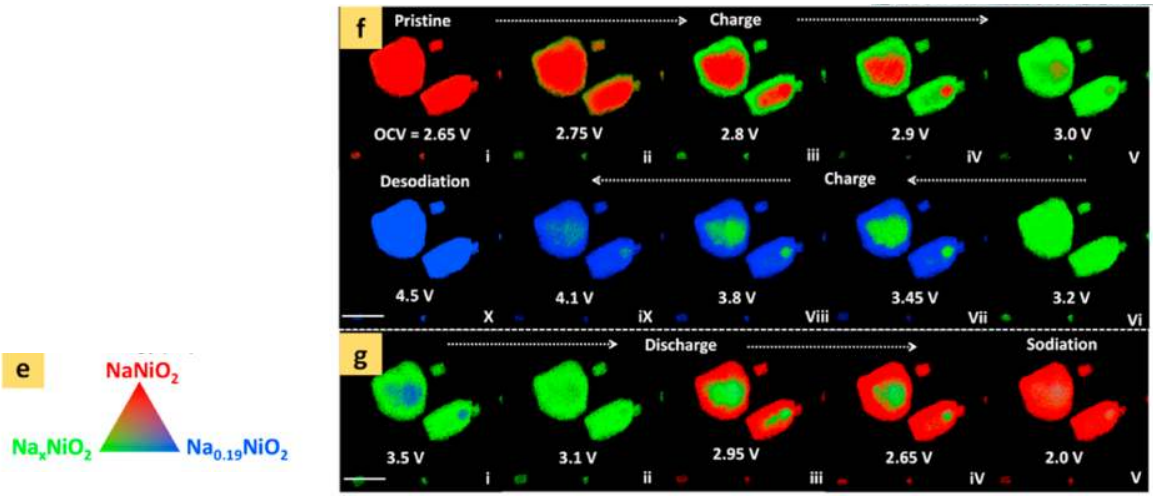

Figure 13 *Operando* hard X-ray spectroscopic imaging of the 2D microstructural evolution of a $NaNiO_2$ cathode. (e) The reference colours indicate the three phases in the chemical maps. (f,g) 2D chemical phase mapping during the first charge and discharge processes. Scale bar: 10 µm. Adapted from Ref. [190] with permission from Elsevier.

5.2. Exploration of failure mechanisms

Most imaging techniques require vacuum conditions, which are not compatible with liquid-based electrolytes. To address this issue, special electrochemical cells were built with either a solid electrolyte (Na_2O/NaOH mixture) or an ionic liquid. Unfortunately, both these electrolytes lead to rapid cell failure. Thus, investigations of failure mechanisms are based on *ex situ* experiments. From FIB/SEM cross-sectional images, Farbod *et al*.[191] observed that the Sn electrode was fully detached from the current collector after 50 cycles, whereas for a Sn–Ge–Sb alloy electrode, the phenomenon was only partial, indicating that the ternary alloy was more mechanically stable. This result was in accordance with the higher volume expansion expected for full sodiation of Sn (425%) compared with that for the ternary system (300%–400%). Additionally, TEM and TOF-SIMS experiments allowed the authors to detect Na segregation at the electrode/current collector interface. The failure mechanism of conversion/alloy-based electrodes was investigated by Song *et al*.[166] using three different Ni/Ni_3S_2 electrode morphologies: i) net-structure nanosheet, ii) clustered network nanostructure, and iii) rod-like nanostructure. The *ex situ* SEM investigation performed after 5, 20, and 50 cycles revealed that the rod-like nanostructure was not damaged by cycling, but this sample delivered a very low specific charge compared with the other morphologies. The two other morphologies were found to agglomerate during cycling while keeping a certain porosity, which is crucial for maintaining the wettability of the materials and thus good electrochemical performance.

5.3. Solid electrolyte interphases at the surface level

It is not easy to investigate the SEI using imaging techniques because it is a highly sensitive material that decomposes easily under beam exposure owing to its polymer nature and its electronic insulator nature. Vogt *et al*.[154] investigated the formation of an SEI on Sn particles using post-mortem SEM coupled with XPS. They demonstrated that the SEI layer becomes thicker and thicker as sodiation proceeds. At the end of sodiation, the particles were found to be completely covered by a thick polymer layer. Washing the electrode revealed the structural damage of the particles, *i.e*. fracturing of the particles owing to large volume changes. Weadock *et al*.[192] investigated the mechanical properties of the SEI formed in different electrolytes by using colloidal probe microscopy. They demonstrated that an inhomogeneous layer develops on a Cu/Si substrate when 1 M $NaPF_6$ in ethylene carbonate / dimethyl carbonate (EC/DEC) is used as the electrolyte (Figure 14). Similarly to Li systems, the SEI was found to be composed of two layers: a soft layer and a hard layer. SEI formation on MoS_2 particles was also followed by *operando* atomic force microscopy (AFM) experiments using a sodium perchlorate-based electrolyte.[193] This study confirmed the results of Weadock *et al*.,[192] revealing that the SEI is composed of two layers with thicknesses ranging between 8 and 54 nm

(average: 20.4 nm). The same experiment on the Li system revealed an average SEI thickness of about 61.8 nm, leading the authors to conclude that the SEI is thinner in Na systems, which explains the better long-term cycling stability in the Na-ion system, as suggested elsewhere.[194]

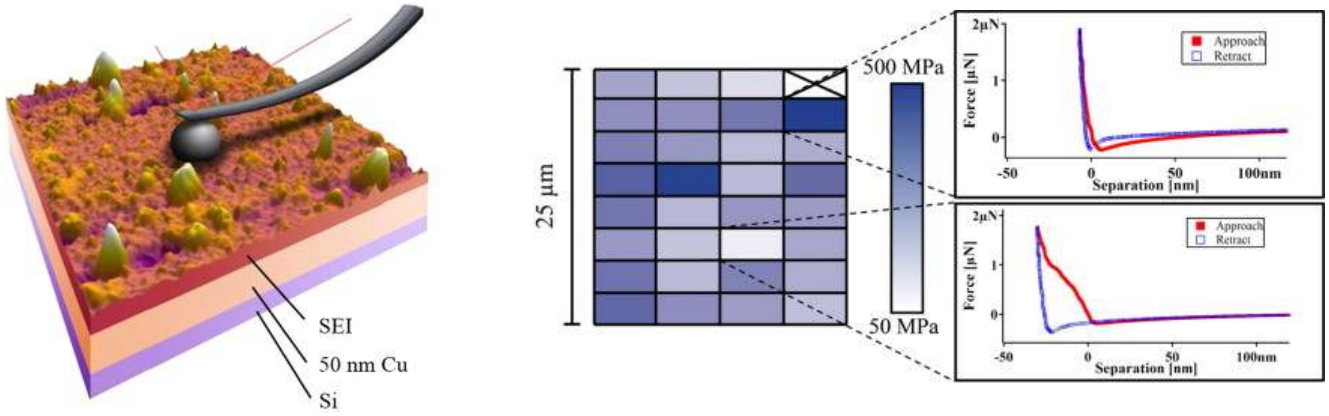

Figure 14 (left) Schematic representation of a solid electrolyte interphase (SEI) layer indented with a colloidal probe, illustrating the structure of the electrode. The side of the SEI image is 10 µm with a height range of 250 nm; (right) Force mapping of the SEI layer. Thirty-two force profiles were measured within a 25 µm × 25 µm area. The Young's modulus at each location in the grid is represented on a gradient scale. Two representative force profiles are shown in the insets. The crossed out space corresponds to anomalous data. Adapted from Ref. [192] with permission from Elsevier.

6. Na-air batteries

The last decade was abounded with tremendous efforts dedicated to post-Li battery chemistries, mainly Li–S and Li-air. Especially the latter proposed technology was seen as a high energy and cost-effective battery of the future. Unfortunately, after years of research, it turned out that most of the time the cells cannot be recharged properly and, thus, the Li-air battery cannot be brought closer to practice. Even though the lithium metal could not have been paired with oxygen because it forms highly unstable LiO_2, which is further irreversibly reduced to Li_2O_2, the concept of the metal-air battery was not completely discarded. Side efforts were devoted to Na-air batteries, in the case of which the oxygen reacting with metal forms a very stable superoxide, NaO_2 that can be reversibly cycled, as reported for the first time in 2013 by Hartmann et al.[195] This pioneering work entailed a great deal of effort dedicated to understanding and further developing both aqueous and non-aqueous Na-air battery systems. Lutz et al.[196], for example, demonstrated that the reversibility of energy storage in non-aqueous Na-air battery is highly influenced by the chemical affinity at the surface of the cathode. Moreover, the choice of the material for the positive electrode defines the morphology of the crystallizing NaO_2, which, in turn, has a strong influence on the electrochemistry. When uncoated carbon-based materials (GDL fibres) are employed the NaO_2 forms cubes, whereas with Au-coated GLD cathodes it forms flakes instead (Figure 15). The former morphology seems more favourable for stable cycling of the non-aqueous Na-air battery.

In the case of aqueous Na-air batteries there has been a lot of work carried out to improve the catalyst for the air electrode. So far employed catalysts, such as VO_2, SnS_2, MnO_2 and $Co_3(PO_4)_2$ were able to reduce the overpotential of the system and to enhance the reversibility of the processes taking place during cycling.[75, 77, 78] The efficient catalyst for metal-air battery need to have, however, a particular morphology to ensure proper air circulation in the electrode. This morphology can be resolved by numerous imaging techniques, e.g. SEM (Figure 16).

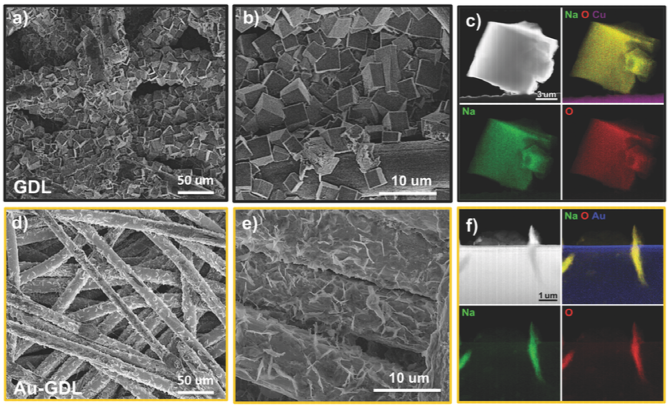

Figure 15 SEM and STEM-EDX data for fully discharged GDL (black) and Au-GDL (yellow) electrodes in DGME electrolyte. a) Low magnification of assembly of NaO_2 cubes covering GDL fibers and b) zoom on interconnected cubes on a GDL fiber. Overview of d) Au-GDL fibers coated by NaO_2 flakes and e) high magnification of 3–5 µm long flakes on Au-GDL fibers. High angle annular dark field - scanning transmission electron microscope (HAADF-STEM) image together with the corresponding elemental maps for c) NaO_2 cubes in the GDL sample and f) Na–O flakes on an Au-GDL fiber. Reproduced from Ref. [196] with permission from John Wiley and Sons.

Of course the research on prospective Na-air batteries is still in its infancy, and there is no doubt that imaging techniques will be more and more often employed to monitor and assess the performance of these type of batteries.[76]

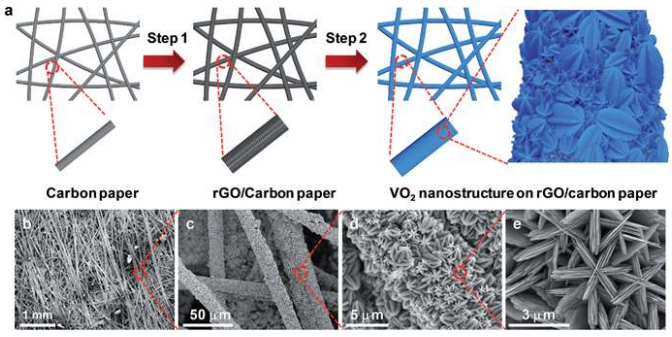

Figure 16 Synthetic scheme and morphology study. (a) Schematic illustration for synthesis of the VGC electrode (b) & (c) low-magnification (d) & (e) high-magnification SEM images of the prepared binder-free VGC electrode. SEM images show the formation of carambola-shaped VO_2 nanostructures on rGO-coated carbon paper. Reproduced from Ref. [77] with permission from The Royal Society of Chemistry

7. All-solid-state Li-ion batteries based on ceramic electrolytes

All-solid-state batteries have been presented as the ideal solution to address i) the safety limitations of conventional Li-ion batteries owing to the flammability of organic electrolytes and ii) the problem of 'low' energy densities by enabling the use of Li metal counter electrodes. Two main categories of 'novel' solid electrolytes have been investigated: oxide-based and sulfide-based electrolytes. In this section, we focus only on oxide-based electrolytes, as sulfide-based materials cannot yet be properly studied by imaging techniques owing to beam damage. The use of imaging techniques for sulfide-based electrolytes is not recommended owing to the highly metastable Li–S bond and the air/moisture sensitivity of these materials (release of H_2S following contact with air/moisture). To date, ceramic-based electrolytes have been widely explored at the material level to improve their ionic conductivities and also at the interface level to improve the voltage window stability. Additionally, efforts have been dedicated to overcoming the issue of dendrite formation when Li metal is used as the counter electrode. As research has been dedicated to the materials side, there are only a few reports on imaging techniques coupled to all-solid-state batteries using ceramic-based electrolytes. The first challenge that arises when investigating solid electrolytes using (S)TEM techniques is beam damage, similar to that observed in Li–S batteries. This damage is mostly caused by fast Li-ion mobility within the solid electrolyte coupled to its low electronic conductivity.

However, Otoyama *et al.*[197] used a Raman imaging technique, which is less sensitive and destructive, to follow the reaction of a composite $LiCoO_2$ electrode coupled to a Li_2S-P_2S_5 solid electrolyte. They examined the system in the pristine state as well as after full delithiation. As shown in Figure 17, the distribution of Li within the composite electrode is not homogeneous. The blue colour (Figure 17b) indicates that the delithiation proceed well through the electrode; however, the black circle indicates an inhomogeneous reaction based on a low SOC for $LiCoO_2$, as can be seen in the individual mapping images in Figure 17c. Indeed, aggregates of $LiCoO_2$ particles are not in proper contact with the solid electrolyte and are thus 'excluded' from the Li pathway. Additionally, more Co_3O_4 is present at the bottom of the image (in direct contact with the solid electrolyte), which indicates that the particles close to the electrode/electrolyte interface have the tendency to be overcharged during cycling. This study revealed the difficulties in obtaining an optimal interface and contact between the active materials and the solid electrolyte when composite electrodes are used. This information is of vital importance for the development of safer all-solid-state batteries employing composite electrodes.

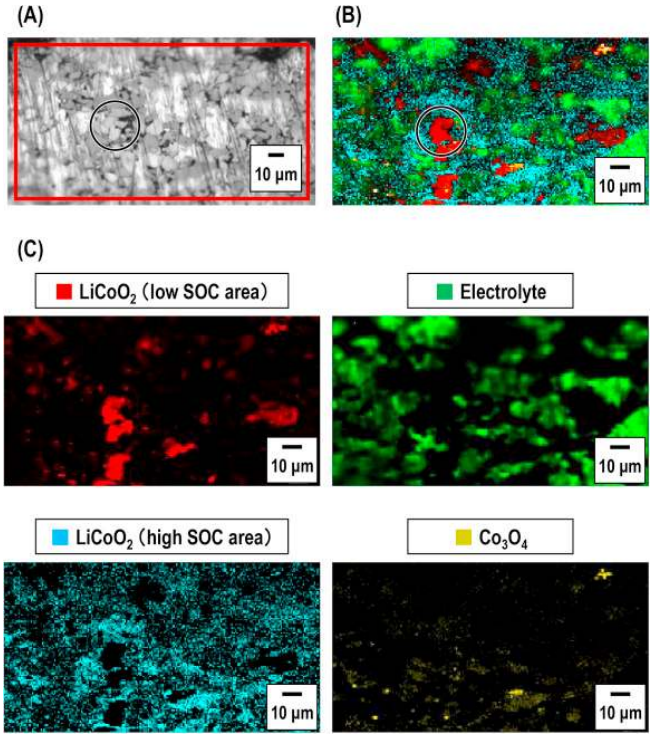

Figure 17 (a) Optical micrograph, (b) mapping image of the $LiCoO_2$ electrode layer after the first charging process, and (c) individual mapping images of $LiCoO_2$, electrolyte, and Co_3O_4. Reproduced from Ref. [197] with permission from Elsevier.

Zhang *et al.*[198] investigated an all-solid-state cell ($LiCoO_2$/$Li_{10}GeP_2S_{12}$/In) using a synchrotron source. The goal of this study was to investigate the mechanical stability of the stack during cycling by using a combination of transmission X-ray tomography, pressure changes, and dilatometry. The results from the pressure and dilatometry measurements showed that the stack experienced a change in volume coupled to an increase in pressure during cycling. Thus, several fractures were expected in the transmission X-ray tomography measurements. Figure 18a shows the difference between the pristine sample and the fully charged sample, as measured by X-ray tomography. The charged electrode was considerably bent compared with the pristine one, indicating that the electrode experienced a volume change during cycling. The consequences of this volume changes can be seen at the edge of the pellet (extreme left side of Figure 18), where several cracks became visible after one charge. Additionally, the impact of pressure on the stack during cycling was examined.

As shown in Figure 18b, increasing the pressure led to densification of the pellet, as the porosity of the charged sample is lower than that of the pristine sample.

This study demonstrated not only that contact between the electrode and electrolyte is vital, but also that a cathode and an anode that undergo minimal volume changes during cycling need to be selected to ensure long-term cycling. Conventional Li-ion batteries based on organic liquid electrolytes can accommodate the breathing of the electrode without any detrimental effects. However, the $LiCoO_2$ cathode, which experiences a volume change of less than 10% upon lithiation, is already a limiting factor, which shows a limitation of the solid-state batteries and the necessity of carrying out further imaging analyses to understand the fracture mechanisms and their impact during cycling.

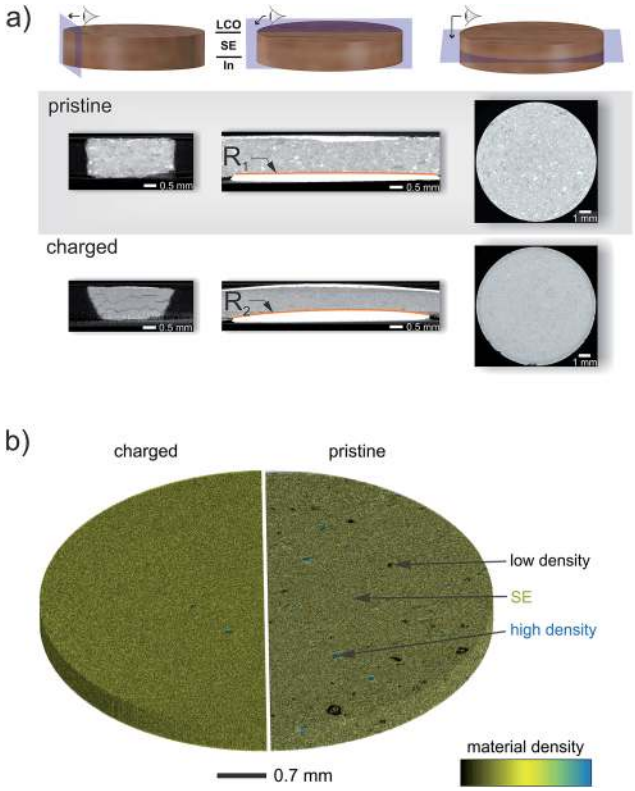

Figure 18 (a) *Ex situ* transmission X-ray tomography of a pristine SSB pellet of $In/Li_{10}GeP_2S_{12}/LiCoO_2$ fabricated by isostatic pressing and of another pellet after the first charge at a current density corresponding to 0.1C. As no external compressive pressure was applied to the pellet during galvanostatic charging, a change in the shape of the cell was observed. The purple planes in the top row indicate the tomography image slices that are shown below, as viewed from above. Bright areas in the grey-scale X-ray tomography images indicate high attenuation of the incoming X-rays, *i.e.* heavy elements or higher material density. Therefore, the bright area on top of each pellet in the middle column corresponds to Li_xCoO_2 in the composite cathode. The very bright area at the bottom of each pellet corresponds to the In metal as anode. The charged pellet was subjected to a strong bending force during charging (middle column), demonstrating the strong pressure build-up and strain generated at the interface of the solid electrolyte and the electrodes. Cracking of the solid electrolyte can be observed at the edges of the charged cell (left column). (b) 3D reconstruction of the *ex situ* synchrotron X-ray tomography data for the same isostatically pressed SSB pellets in the pristine state (right) and after charge (left). No external compressive pressure was exerted on the pellet during the charge process. The inhomogeneities present in the pristine state (black and blue areas) vanish after the charge, which is accompanied by a decrease in the porosity of the solid electrolyte. This behaviour might be due to volume expansion of the In–Li alloy at the anode and of $LiCoO_2$ at the cathode during the charge process, which is in good agreement with the pressure monitoring results. Reproduced from Ref. [198] with permission from The Royal Society of Chemistry.

The interfacial issue between the electrode and the electrolyte has also been reported for ceramic-based all-solid-state batteries. Kim *et al.*[199] studied the interfacial layer formed between $Li_7La_3Zr_2O_{12}$ (LLZO) and $LiCoO_2$ during thin film deposition using a combination of microscopy techniques. Using cross-sectional TEM analysis (Figure 19) coupled to EDX measurements, they found a diffusion gradient between the cathode material and the solid electrolyte at the interface. This gradient is believed to be formed '*in situ*' through mutual diffusion of elements during deposition of the film at high temperatures. Unfortunately, this layer was found to be mostly insulating (composed of La, Co, and O), which limits the electrochemical performance. Removal of this layer or at least decreasing its thickness should allow cycling of solid-state batteries with LLZO as the solid electrolyte.

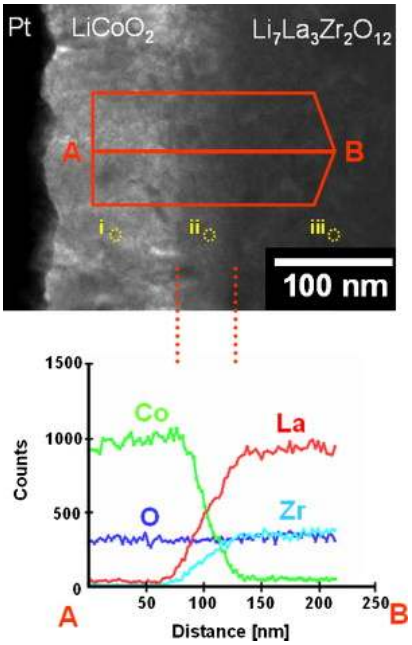

Figure 19 (a) Cross-sectional TEM image of an LLZO/$LiCoO_2$ thin film interface and (b) EDS line profiles of the region indicated by the red arrow in the direction A–B. The broken red lines indicate the reaction layer at the LLZO/$LiCoO_2$ interface. Reproduced from Ref. [199] with permission from Elsevier.

8. Conclusion

As demonstrated in this review, imaging techniques are widely used to explore all types of post-Li batteries. Like other characterization techniques, imaging techniques offer several advantages and drawbacks, as summarized by the following questions and answers.

Can we rely on ex situ sample investigations?

The debate about *ex situ* investigations compared with *operando* experiments is still on-going in the community owing to the nature of many *ex situ* samples which are air/moisture sensitive and subject to relaxation prior to analysis.[200] Although the 'bulk' morphology of a sample may not evolve during *ex situ* analysis, its structure will be affected owing to the metastable character of the extracted phase. This

observation is particularly true for alloy/conversion-based materials. Similar to Li_xSn,[201] the sodiated Na_xSn[202] phases exhibit a metastable equilibrium; therefore, their identification using *ex situ* techniques is unlikely. The conversion-based material CuO[184] has been investigated by *ex situ* TEM and *operando* TEM. In the former case, the end sodiation product was found to be a ternary phase (NaCuO). In the latter case, the end sodiation product was identified as a mixture of Na_2O and Cu_2O, raising doubts about the goal of imaging techniques for *ex situ* investigations. Moreover, *operando* experiments can provide additional information about Na diffusion[175] and the kinetics[186] of the electrode material.

To what extent does beam damage affect data interpretation?

One has to be cautious in data interpretation because imaging techniques are often laden with artefacts and other limitations. Therefore, subtle differences between two or more images of the same material may not be a result of the electrochemistry but may instead be induced by beam damage,[123] leading to possible misinterpretation of the electrochemical degradation mechanism. Furthermore, the beam set-up should be carefully chosen, depending of what one wants to observe. Some materials, such as sulfur and phosphorus, evaporate under the beam, as do decomposition layers that are made of polymers, such as the SEI. Thus, a subtle balance has to be found to obtain suitable images with possibly high resolution while maintaining the material or polymer properties. In doubt, the resolution should be sacrificed in favour of lower beam energy.

Where are the limits of imaging technique applied to batteries?

While 'a picture is worth a thousand words', images of electrodes or other battery components should not be over-interpreted. Although advanced and mostly precise, imaging techniques have limitations, especially with regards to tracking highly sensitive materials and mechanically unstable soft passivation layers, such as the SEI.[193] In the case of *ex situ* measurements, despite the mild conditions applied during analysis, the SEI can be easily damaged by the beam. For *operando* measurements, many more parameters and obstacles need to be considered.[184, 200,] For instance, because high vacuum is required for SEM and TEM analyses, conventional organic-based electrolytes cannot be used. Instead, a mixture of Na_2O and NaOH is used as an electrolyte, which however strongly influences the chemical composition of the SEI and, hence, the obtained results.[180]

Overall, imaging techniques provide crucial information, mainly about morphological modifications, possible stresses that can occur in batteries, and the electrode/electrolyte interface. Moreover, imaging techniques are often coupled with elemental analysis or mapping to obtain a complete information about the different reactions occurring in batteries. While the results provided by imaging techniques alone are useful, the observations and conclusions extracted from such analyses should be combined with the results from a number of other methods.

Conflicts of interest

There are no conflicts to declare.

Notes and references

1. K. Ozawa, *Solid State Ionics*, 1994, **69**, 212-221.
2. J. M. Tarascon and M. Armand, *Nature*, 2001, **414**, 359-367.
3. J. O. Besenhard, J. Yang and M. Winter, *J. Power Sources*, 1997, **68**, 87-90.
4. J.-M. Tarascon, S. Grugeon, M. Morcrette, S. Laruelle, P. Rozier and P. Poizot, *Comptes Rendus Chimie*, 2005, **8**, 9-15.
5. R. A. Huggins, *Journal of Power Sources*, 1999, **81–82**, 13-19.
6. K. Kushida, K. Kuriyama and T. Nozaki, *Applied Physics Letters*, 2002, **81**, 5066-5068.
7. M. Armand and J. M. Tarascon, *Nature*, 2008, **451**, 652-657.
8. E. J. Berg, C. Villevieille, D. Streich, S. Trabesinger and P. Novak, *J. Electrochem. Soc.*, 2015, **162**, A2468-A2475.
9. S. H. Kang, P. Kempgens, S. Greenbaum, A. J. Kropf, K. Amine and M. M. Thackeray, *J. Mater. Chem.*, 2007, **17**, 2069-2077.
10. M. M. Thackeray, S. H. Kang, C. S. Johnson, J. T. Vaughey, R. Benedek and S. A. Hackney, *J. Mater. Chem.*, 2007, **17**, 3112-3125.
11. E. Levi and D. Aurbach, *Solid State Ionics*, 2014, **257**, 1-8.
12. F. Amalraj, M. Talianker, B. Markovsky, L. Burlaka, N. Leifer, G. Goobes, E. M. Erickson, O. Haik, J. Grinblat, E. Zinigrad, D. Aurbach, J. K. Lampert, J. Y. Shin, M. Schulz-Dobrick and A. Garsuch, *J. Electrochem. Soc.*, 2013, **160**, A2220-A2233.
13. M. M. Thackeray, C. S. Johnson, J. T. Vaughey, N. Li and S. A. Hackney, *J. Mater. Chem.*, 2005, **15**, 2257-2267.
14. N. Tran, L. Croguennec, M. Menetrier, F. Weill, P. Biensan, C. Jordy and C. Delmas, *Chemistry of Materials*, 2008, **20**, 4815-4825.
15. E. Castel, E. J. Berg, M. El Kazzi, P. Novák and C. Villevieille, *Chemistry of Materials*, 2014, **26**, 5051-5057.
16. Y. Li, M. Bettge, B. Polzin, Y. Zhu, M. Balasubramanian and D. P. Abraham, *J. Electrochem. Soc.*, 2013, **160**, A3006-A3019.
17. T. Liu, A. Garsuch, F. Chesneau and B. L. Lucht, *J. Power Sources*, 2014, **269**, 920-926.
18. M. Kunduraci and G. G. Amatucci, *J. Electrochem. Soc.*, 2006, **153**, A1345-A1352.
19. W. Zhu, D. Liu, J. Trottier, P. Hovington, C. Gagnon, A. Guerfi, K. Zaghib, A. Mauger, H. Groult and C. M. Julien, *Intercalation Compounds for Rechargable Batteries*, 2014, **58**, 35-40.
20. M. X. Lin, L. B. Ben, Y. Sun, H. Wang, Z. Z. Yang, L. Gu, X. Q. Yu, X. Q. Yang, H. F. Zhao, R. Yu, M. Armand and X. J. Huang, *Chemistry of Materials*, 2015, **27**, 292-303.
21. C. Villevieille, P. Lanz, C. Bunzli and P. Novak, *J. Mater. Chem. A*, 2014, **2**, 6488-6493.
22. L. Boulet-Roblin, M. El Kazzi, P. Novak and C. Villevieille, *J. Electrochem. Soc.*, 2015, **162**, A1297-A1300.

23. L. Boulet-Roblin, P. Borel, D. Sheptyakov, C. Tessier, P. Novak and C. Villevieille, *J. Phys. Chem. C*, 2016, **120**, 17268-17273.
24. Y. V. Mikhaylik and J. R. Akridge, *Journal of The Electrochemical Society*, 2004, **151**, A1969-A1976.
25. Y. Kato, S. Hori, T. Saito, K. Suzuki, M. Hirayama, A. Mitsui, M. Yonemura, H. Iba and R. Kanno, *Nature Energy*, 2016, **1**, 16030.
26. X. Ji, K. T. Lee and L. F. Nazar, *Nature Materials*, 2009, **8**, 500-506.
27. J. Wang, L. Liu, Z. Ling, J. Yang, C. Wan and C. Jiang, *Electrochimica Acta*, 2003, **48**, 1861-1867.
28. C. Liang, N. J. Dudney and J. Y. Howe, *Chemistry of Materials*, 2009, **21**, 4724-4730.
29. S. Thieme, J. Bruckner, I. Bauer, M. Oschatz, L. Borchardt, H. Althues and S. Kaskel, *Journal of Materials Chemistry A*, 2013, **1**, 9225-9234.
30. B. Ding, C. Yuan, L. Shen, G. Xu, P. Nie and X. Zhang, *Chemistry – A European Journal*, 2013, **19**, 1013-1019.
31. G. Xu, B. Ding, P. Nie, L. Shen, H. Dou and X. Zhang, *ACS Applied Materials & Interfaces*, 2014, **6**, 194-199.
32. Z. Gong, Q. Wu, F. Wang, X. Li, X. Fan, H. Yang and Z. Luo, *RSC Advances*, 2016, **6**, 37443-37451.
33. Z. Xiao, Z. Yang, H. Nie, Y. Lu, K. Yang and S. Huang, *Journal of Materials Chemistry A*, 2014, **2**, 8683-8689.
34. C. Villevieille and P. Novak, *Journal of Materials Chemistry A*, 2013, **1**, 13089-13092.
35. J. Wang, J. Yang, J. Xie and N. Xu, *Advanced Materials*, 2002, **14**, 963-965.
36. S.-M. Zhang, Q. Zhang, J.-Q. Huang, X.-F. Liu, W. Zhu, M.-Q. Zhao, W.-Z. Qian and F. Wei, *Particle & Particle Systems Characterization*, 2013, **30**, 158-165.
37. Y. Yang, G. Yu, J. J. Cha, H. Wu, M. Vosgueritchian, Y. Yao, Z. Bao and Y. Cui, *ACS Nano*, 2011, **5**, 9187-9193.
38. J.-Q. Huang, Q. Zhang, H.-J. Peng, X.-Y. Liu, W.-Z. Qian and F. Wei, *Energy & Environmental Science*, 2014, **7**, 347-353.
39. I. Bauer, S. Thieme, J. Bruckner, H. Althues and S. Kaskel, *J. Power Sources*, 2014, **251**, 417-422.
40. J. Conder, S. Urbonaite, D. Streich, P. Novak and L. Gubler, *RSC Advances*, 2015, **5**, 79654-79660.
41. J. Conder, A. Forner-Cuenca, E. M. Gubler, L. Gubler, P. Novák and S. Trabesinger, *ACS Applied Materials & Interfaces*, 2016, **8**, 18822-18831.
42. M. Gu, J. Lee, Y. Kim, J. S. Kim, B. Y. Jang, K. T. Lee and B.-S. Kim, *RSC Advances*, 2014, **4**, 46940-46946.
43. J. Park, B.-C. Yu, J. S. Park, J. W. Choi, C. Kim, Y.-E. Sung and J. B. Goodenough, *Adv. Energy Mater.*, 2017, **7**, 1602567-n/a.
44. Y. Mi, W. Liu, X. Li, J. Zhuang, H. Zhou and H. Wang, *Nano Res.*, 2017, **10**, 3698-3705.
45. G. Babu, K. Ababtain, K. Y. S. Ng and L. M. R. Arava, *Sci Rep*, 2015, **5**, 8763.
46. Y.-S. Su and A. Manthiram, *Chemical Communications*, 2012, **48**, 8817-8819.
47. S.-H. Chung and A. Manthiram, *Chemical Communications*, 2014, **50**, 4184-4187.
48. X. Han, Y. Xu, X. Chen, Y.-C. Chen, N. Weadock, J. Wan, H. Zhu, Y. Liu, H. Li, G. Rubloff, C. Wang and L. Hu, *Nano Energy*, 2013, **2**, 1197-1206.
49. D. Aurbach, E. Pollak, R. Elazari, G. Salitra, C. S. Kelley and J. Affinito, *Journal of The Electrochemical Society*, 2009, **156**, A694-A702.
50. J.-S. Kim, T. H. Hwang, B. G. Kim, J. Min and J. W. Choi, *Advanced Functional Materials*, 2014, **24**, 5359-5367.
51. Y. Yang, G. Zheng and Y. Cui, *Energy & Environmental Science*, 2013, **6**, 1552-1558.
52. http://www.sionpower.com/ *accessed July 27, 2016*.
53. http://www.oxisenergy.com/ *accessed July 27, 2016*.
54. N. Yabuuchi, K. Kubota, M. Dahbi and S. Komaba, *Chem Rev*, 2014, **114**, 11636-11682.
55. Y. U. Park, D. H. Seo, H. S. Kwon, B. Kim, J. Kim, H. Kim, I. Kim, H. I. Yoo and K. Kang, *J Am Chem Soc*, 2013, **135**, 13870-13878.
56. C. Masquelier and L. Croguennec, *Chem Rev*, 2013, **113**, 6552-6591.
57. S. Yu, Y. Li, Y. Lu, B. Xu, Q. Wang, M. Yan and Y. Jiang, *Journal of Power Sources*, 2015, **275**, 45-49.
58. W. Luo, M. Allen, V. Raju and X. Ji, *Advanced Energy Materials*, 2014, **4**, 1400554.
59. C. Delmas, C. Fouassier and P. Hagenmuller, *Physica B+C*, 1980, **99**.
60. I. Hasa, D. Buchholz, S. Passerini and J. Hassoun, *ACS Appl Mater Interfaces*, 2015, **7**, 5206-5212.
61. M. Keller, C. Vaalma, D. Buchholz and S. Passerini, *Chem Electro Chem*, 2016, **3**.
62. J. Y. Hwang, S. T. Myung and Y. K. Sun, *Chem Soc Rev*, 2017, **46**, 3529-3614.
63. A. Ponrouch and M. R. Palacín, *Electrochemistry Communications*, 2015, **54**, 51-54.
64. K.-l. Hong, L. Qie, R. Zeng, Z.-q. Yi, W. Zhang, D. Wang, W. Yin, C. Wu, Q.-j. Fan, W.-x. Zhang and Y.-h. Huang, *Journal of Materials Chemistry A*, 2014, **2**, 12733.
65. H. Usui, S. Yoshioka, K. Wasada, M. Shimizu and H. Sakaguchi, *ACS Appl Mater Interfaces*, 2015, **7**, 6567-6573.
66. A. Darwiche, M. T. Sougrati, B. Fraisse, L. Stievano and L. Monconduit, *Electrochemistry Communications*, 2013, **32**, 18-21.
67. C. Marino, T. Block, R. Pöttgen and C. Villevieille, *Journal of Power Sources*, 2017, **342**, 616-622.
68. L. O. Vogt and C. Villevieille, *J. Mater. Chem. A*, 2016, **4**, 19116-19122.
69. L. O. Vogt and C. Villevieille, *J. Mater. Chem. A*, 2017, **5**, 3865-3874.
70. L. O. Vogt, M. El Kazzi, E. J. Berg, S. P. Villar, P. Novak and C. Villevieille, *Chemistry of Materials*, 2015, **27**, 1210-1216.
71. C. Kim, K.-Y. Lee, I. Kim, J. Park, G. Cho, K.-W. Kim, J.-H. Ahn and H.-J. Ahn, *Journal of Power Sources*, 2016, **317**, 153-158.
72. A. Darwiche, C. Marino, M. T. Sougrati, B. Fraisse, L. Stievano and L. Monconduit, *J Am Chem Soc*, 2012, **134**, 20805-20811.
73. P. Hartmann, C. L. Bender, M. Vracar, A. K. Duerr, A. Garsuch, J. Janek and P. Adelhelm, *Nat. Mater.*, 2013, **12**, 228-232.
74. W.-W. Yin and Z.-W. Fu, *ChemCatChem*, 2017, **9**, 1545-1553.
75. B. Senthilkumar, Z. Khan, S. Park, I. Seo, H. Ko and Y. Kim, *J. Power Sources*, 2016, **311**, 29-34.
76. Z. Khan, S. Park, S. M. Hwang, J. Yang, Y. Lee, H.-K. Song, Y. Kim and H. Ko, *NPG Asia Mater.*, 2016, **8**, e294.
77. Z. Khan, B. Senthilkumar, S. O. Park, S. Park, J. Yang, J. H. Lee, H.-K. Song, Y. Kim, S. K. Kwak and H. Ko, *J. Mater. Chem. A*, 2017, **5**, 2037-2044.

78. Z. Khan, N. Parveen, S. A. Ansari, S. T. Senthilkumar, S. Park, Y. Kim, M. H. Cho and H. Ko, *Electrochim. Acta*, 2017, **257**, 328-334.
79. C. L. Tsai, V. Roddatis, C. V. Chandran, Q. L. Ma, S. Uhlenbruck, M. Bram, P. Heitjans and O. Guillon, *ACS Appl. Mater. Interfaces*, 2016, **8**, 10617-10626.
80. P. Novák, J. C. Panitz, F. Joho, M. Lanz, R. Imhof and M. Coluccia, *J. Power Sources*, 2000, **90**, 52-58.
81. S. F. Amalraj and D. Aurbach, *J Solid State Electrochem*, 2011, **15**, 877-890.
82. J. Vetter, L. J. Hardwick, A. Würsig, M. Holzapfel, O. D. Schneider, J. Ufheil and P. Novák, *ECS Transactions*, 2007, **3**, 29-43.
83. http://www.eng.utah.edu/~lzang/images/Lecture_3_conventional-Microscope.pdf.
84. http://www.spectral.se/spectral.nsf/f164f3e9b82f0febc1256dcc004611c1/d4a98a973f4e0290c12571e300376e06/$FILE/208%20Why%20STEM%20Not%20TEM.pdf.
85. Y.-J. Choi, Y.-D. Chung, C.-Y. Baek, K.-W. Kim, H.-J. Ahn and J.-H. Ahn, *Journal of Power Sources*, 2008, **184**, 548-552.
86. Y. Wang, Y. Huang, W. Wang, C. Huang, Z. Yu, H. Zhang, J. Sun, A. Wang and K. Yuan, *Electrochimica Acta*, 2009, **54**, 4062-4066.
87. H. S. Ryu, Z. Guo, H. J. Ahn, G. B. Cho and H. Liu, *Journal of Power Sources*, 2009, **189**, 1179-1183.
88. L. Yuan, X. Qiu, L. Chen and W. Zhu, *Journal of Power Sources*, 2009, **189**, 127-132.
89. S. Walus, C. Barchasz, J.-F. Colin, J.-F. Martin, E. Elkaim, J.-C. Lepretre and F. Alloin, *Chemical Communications*, 2013, **49**, 7899-7901.
90. J. Nelson, S. Misra, Y. Yang, A. Jackson, Y. Liu, H. Wang, H. Dai, J. C. Andrews, Y. Cui and M. F. Toney, *Journal of the American Chemical Society*, 2012, **134**, 6337-6343.
91. N. A. Cañas, S. Wolf, N. Wagner and K. A. Friedrich, *Journal of Power Sources*, 2013, **226**, 313-319.
92. S. Waluś, C. Barchasz, R. Bouchet, J.-C. Leprêtre, J.-F. Colin, J.-F. Martin, E. Elkaïm, C. Baehtz and F. Alloin, *Advanced Energy Materials*, 2015, **5**, 1500165.
93. Y. Mao, G. Li, Y. Guo, Z. Li, C. Liang, X. Peng and Z. Lin, *Nature Communications*, 2017, **8**, 14628.
94. S.-H. Chung and A. Manthiram, *Electrochemistry Communications*, 2014, **38**, 91-95.
95. S.-H. Chung and A. Manthiram, *Journal of Materials Chemistry A*, 2013, **1**, 9590-9596.
96. D.-W. Wang, G. Zhou, F. Li, K.-H. Wu, G. Q. Lu, H.-M. Cheng and I. R. Gentle, *Physical Chemistry Chemical Physics*, 2012, **14**, 8703-8710.
97. J.-W. Choi, G. Cheruvally, D.-S. Kim, J.-H. Ahn, K.-W. Kim and H.-J. Ahn, *Journal of Power Sources*, 2008, **183**, 441-445.
98. R. Elazari, G. Salitra, Y. Talyosef, J. Grinblat, C. Scordilis-Kelley, A. Xiao, J. Affinito and D. Aurbach, *Journal of The Electrochemical Society*, 2010, **157**, A1131-A1138.
99. C. Raiß, K. Peppler, J. Janek and P. Adelhelm, *Carbon*, 2014, **79**, 245-255.
100. P. Echlin, *Low-Temperature Microscopy and Analysis*, Springer US, 2013.
101. R. F. Egerton, P. Li and M. Malac, *Micron*, 2004, **35**, 399-409.
102. N. D. B., *Icarus*, 1987, **72**, 1-34.
103. W. Li, Q. Zhang, G. Zheng, Z. W. Seh, H. Yao and Y. Cui, *Nano Letters*, 2013, **13**, 5534-5540.
104. W. Zhou, Y. Yu, H. Chen, F. J. DiSalvo and H. D. Abruña, *Journal of the American Chemical Society*, 2013, **135**, 16736-16743.
105. B. D. A. Levin, M. J. Zachman, J. G. Werner, U. Wiesner, L. F. Kourkoutis and D. A. Muller, *Microsc. microanal.*, 2014, **20**, 446-447.
106. B. D. A. Levin, M. J. Zachman, J. G. Werner, R. Sahore, K. X. Nguyen, Y. Han, B. Xie, L. Ma, L. A. Archer, E. P. Giannelis, U. Wiesner, L. F. Kourkoutis and D. A. Muller, *Microscopy and Microanalysis*, 2017, **23**, 155-162.
107. W. Zhou, X. Xiao, M. Cai and L. Yang, *Nano Letters*, 2014, **14**, 5250-5256.
108. H. Kim, J. T. Lee, A. Magasinski, K. Zhao, Y. Liu and G. Yushin, *Advanced Energy Materials*, 2015, **5**, 1501306-n/a.
109. Z. Wei Seh, W. Li, J. J. Cha, G. Zheng, Y. Yang, M. T. McDowell, P.-C. Hsu and Y. Cui, *Nature Communications*, 2013, **4**, 1331.
110. B. D. A. Levin, M. J. Zachman, J. G. Werner, R. Sahore, K. X. Nguyen, Y. Han, B. Xie, L. Ma, L. A. Archer, E. P. Giannelis, U. Wiesner, L. F. Kourkoutis and D. A. Muller, *Microsc. microanal.*, 2017, **23**, 155-162.
111. R. Sahore, L. P. Estevez, A. Ramanujapuram, F. J. DiSalvo and E. P. Giannelis, *Journal of Power Sources*, 2015, **297**, 188-194.
112. R. Sahore, B. D. A. Levin, M. Pan, D. A. Muller, F. J. DiSalvo and E. P. Giannelis, *Advanced Energy Materials*, 2016, **6**, 1600134-n/a.
113. A. Yermukhambetova, C. Tan, S. R. Daemi, Z. Bakenov, J. A. Darr, D. J. L. Brett and P. R. Shearing, *Sci Rep*, 2016, **6**, 35291.
114. L. Zielke, T. Hutzenlaub, D. R. Wheeler, C. W. Chao, I. Manke, A. Hilger, N. Paust, R. Zengerle and S. Thiele, *Adv. Energy Mater.*, 2015, **5**.
115. Y. Yang, S. Risse, S. Mei, C. J. Jafta, Y. Lu, C. Stöcklein, N. Kardjilov, I. Manke, J. Gong, Z. Kochovski and M. Ballauff, *Energy Storage Materials*, 2017, **9**, 96-104.
116. S. Risse, C. J. Jafta, Y. Yang, N. Kardjilov, A. Hilger, I. Manke and M. Ballauff, *Physical Chemistry Chemical Physics*, 2016, **18**, 10630-10636.
117. D. Schröder, C. L. Bender, T. Arlt, M. Osenberg, A. Hilger, S. Risse, M. Ballauff, I. Manke and J. Janek, *Journal of Physics D: Applied Physics*, 2016, **49**, 404001.
118. L. Zielke, C. Barchasz, S. Waluś, F. Alloin, J. C. Leprêtre, A. Spettl, V. Schmidt, A. Hilger, I. Manke, J. Banhart, R. Zengerle and S. Thiele, *Sci Rep*, 2015, **5**, 10921.
119. G. Tonin, G. Vaughan, R. Bouchet, F. Alloin, M. Di Michiel, L. Boutafa, J.-F. Colin and C. Barchasz, *Sci Rep*, 2017, **7**, 2755.
120. A. Etiemble, N. Besnard, A. Bonnin, J. Adrien, T. Douillard, P. Tran-Van, L. Gautier, J.-C. Badot, E. Maire and B. Lestriez, *Journal of Materials Science*, 2017, **52**, 3576-3596.
121. R. Moroni, M. Börner, L. Zielke, M. Schroeder, S. Nowak, M. Winter, I. Manke, R. Zengerle and S. Thiele, *Scientific Reports*, 2016, **6**, 30109.
122. P. Pietsch, M. Hess, W. Ludwig, J. Eller and V. Wood, *Scientific Reports*, 2016, **6**, 27994.
123. J. Nelson, Y. Yang, S. Misra, J. C. Andrews, Y. Cui and M. F. Toney, 2013.

124. H. Wang, Y. Yang, Y. Liang, J. T. Robinson, Y. Li, A. Jackson, Y. Cui and H. Dai, *Nano Letters*, 2011, **11**, 2644-2647.
125. C. Villevieille and P. Novak, *J. Mater. Chem. A*, 2013, **1**, 13089-13092.
126. J. Conder, R. Bouchet, S. Trabesinger, C. Marino, L. Gubler and C. Villevieille, *Nature Energy*, 2017, **2**.
127. S. Walus, C. Barchasz, J. F. Colin, J. F. Martin, E. Elkaim, J. C. Lepretre and F. Alloin, *Chem. Commun.*, 2013, **49**, 7899-7901.
128. C. Villevieille, T. Sasaki and P. Novak, *RSC Adv.*, 2014, **4**, 6782-6789.
129. in *Understanding Batteries*, eds. R. M. Dell and D. A. J. Rand, The Royal Society of Chemistry, 2001, DOI: 10.1039/9781847552228-00143, pp. 143-162.
130. Y. Matsuda, M. Ishikawa, S. Yoshitake and M. Morita, *Journal of Power Sources*, 1995, **54**, 301-305.
131. Y. Matsuda and M. Sekiya, *Journal of Power Sources*, 1999, **81–82**, 759-761.
132. M. Ishikawa, S.-i. Machino and M. Morita, *Journal of Electroanalytical Chemistry*, 1999, **473**, 279-284.
133. Y. Lu, Z. Tu and L. A. Archer, *Nat Mater*, 2014, **13**, 961-969.
134. R. Bouchet, S. Maria, R. Meziane, A. Aboulaich, L. Lienafa, J.-P. Bonnet, T. N. T. Phan, D. Bertin, D. Gigmes, D. Devaux, R. Denoyel and M. Armand, *Nat Mater*, 2013, **12**, 452-457.
135. G. Zheng, S. W. Lee, Z. Liang, H.-W. Lee, K. Yan, H. Yao, H. Wang, W. Li, S. Chu and Y. Cui, *Nature Nanotechnology*, 2014, **9**, 618-623.
136. Y. Liu, D. Lin, Z. Liang, J. Zhao, K. Yan and Y. Cui, *Nature Communications*, 2016, **7**, 10992.
137. D. Lin, Y. Liu, Z. Liang, H.-W. Lee, J. Sun, H. Wang, K. Yan, J. Xie and Y. Cui, *Nature Nanotechnology*, 2016, **11**, 626-632.
138. G. Zheng, S. W. Lee, Z. Liang, H.-W. Lee, K. Yan, H. Yao, H. Wang, W. Li, S. Chu and Y. Cui, *Nat Nano*, 2014, **9**, 618-623.
139. K. N. Wood, E. Kazyak, A. F. Chadwick, K.-H. Chen, J.-G. Zhang, K. Thornton and N. P. Dasgupta, *ACS Central Science*, 2016, **2**, 790-801.
140. X. Wang, M. Zhang, J. Alvarado, S. Wang, M. Sina, B. Lu, J. Bouwer, W. Xu, J. Xiao, J.-G. Zhang, J. Liu and Y. S. Meng, *Nano Letters*, 2017, DOI: 10.1021/acs.nanolett.7b03606.
141. S. Frisco, D. X. Liu, A. Kumar, J. F. Whitacre, C. T. Love, K. E. Swider-Lyons and S. Litster, *ACS Applied Materials & Interfaces*, 2017, **9**, 18748-18757.
142. J.-H. Cheng, A. A. Assegie, C.-J. Huang, M.-H. Lin, A. M. Tripathi, C.-C. Wang, M.-T. Tang, Y.-F. Song, W.-N. Su and B. J. Hwang, *The Journal of Physical Chemistry C*, 2017, **121**, 7761-7766.
143. F. Sun, R. Moroni, K. Dong, H. Markötter, D. Zhou, A. Hilger, L. Zielke, R. Zengerle, S. Thiele, J. Banhart and I. Manke, *ACS Energy Letters*, 2017, **2**, 94-104.
144. W. Xu, J. Wang, F. Ding, X. Chen, E. Nasybulin, Y. Zhang and J.-G. Zhang, *Energy & Environmental Science*, 2014, **7**, 513-537.
145. K. Zhang, G.-H. Lee, M. Park, W. Li and Y.-M. Kang, *Advanced Energy Materials*, 2016, **6**, 1600811.
146. G. Bieker, M. Winter and P. Bieker, *Physical Chemistry Chemical Physics*, 2015, **17**, 8670-8679.
147. D. Aurbach, E. Zinigrad, H. Teller and P. Dan, *J. Electrochem. Soc.*, 2000, **147**, 1274-1279.
148. L. Grande, E. Paillard, G.-T. Kim, S. Monaco and S. Passerini, *International Journal of Molecular Sciences*, 2014, **15**, 8122-8137.
149. W. Li, H. Yao, K. Yan, G. Zheng, Z. Liang, Y.-M. Chiang and Y. Cui, *Nat. Commun.*, 2015, **6**, 7436.
150. J. J. Braconnier, C. Delmas and P. Hagenmuller, *Mat. Res. Bull.*, 1980, **15**.
151. K. Kubota and S. Komaba, *Journal of The Electrochemical Society*, 2015, **162**, A2538-A2550.
152. M. Dahbi, M. Kiso, K. Kubota, T. Horiba, T. Chafik, K. Hida, T. Matsuyama and S. Komaba, *J. Mater. Chem. A*, 2017, **5**, 9917-9928.
153. J. Cui, S. Yao and J. K. Kim, *Energy storage materials*, 2017, **7**.
154. L. O. Vogt, M. El Kazzi, E. Jämstorp Berg, S. Pérez Villar, P. Novák and C. Villevieille, *Chemistry of Materials*, 2015, **27**, 1210-1216.
155. H. Moriwake, A. Kuwabara, C. A. J. Fisher and Y. Ikuhara, *RSC Adv.*, 2017, **7**, 36550-36554.
156. S. Birgisson, Y. Shen and B. B. Iversen, *Chem Commun (Camb)*, 2017, **53**, 1160-1163.
157. V. M. Kovrugin, J.-N. Chotard, F. Fauth, A. Jamali, R. David and C. Masquelier, *J. Mater. Chem. A*, 2017, **5**, 14365-14376.
158. J. Sottmann, F. L. M. Bernal, K. V. Yusenko, M. Herrmann, H. Emerich, D. S. Wragg and S. Margadonna, *Electrochimica Acta*, 2016, **200**, 305-313.
159. G. L. Xu, T. Sheng, L. Chong, T. Ma, C. J. Sun, X. Zuo, D. J. Liu, Y. Ren, X. Zhang, Y. Liu, S. M. Heald, S. G. Sun, Z. Chen and K. Amine, *Nano Lett*, 2017, **17**, 953-962.
160. C. Marino, T. Block, R. Pottgen and C. Villevieille, *J. Power Sources*, 2017, **342**, 616-622.
161. J. M. Stratford, M. Mayo, P. K. Allan, O. Pecher, O. J. Borkiewicz, K. M. Wiaderek, K. W. Chapman, C. J. Pickard, A. J. Morris and C. P. Grey, *J Am Chem Soc*, 2017, **139**, 7273-7286.
162. C. Marino, N. Dupre and C. Villevieille, *J. Power Sources*, 2017, **365**, 339-347.
163. G. Singh, J. M. López del Amo, M. Galceran, S. Pérez-Villar and T. Rojo, *J. Mater. Chem. A*, 2015, **3**, 6954-6961.
164. R. Berthelot, D. Carlier and C. Delmas, *Nat Mater*, 2011, **10**, 74-80.
165. Y. Fang, Q. Liu, L. Xiao, X. Ai, H. Yang and Y. Cao, *ACS Appl Mater Interfaces*, 2015, **7**, 17977-17984.
166. X. Song, X. Li, Z. Bai, B. Yan, D. Li and X. Sun, *Nano Energy*, 2016, **26**, 533-540.
167. L. O. Vogt, C. Marino and C. Villevieille, *Chimia (Aarau)*, 2015, **69**, 729-733.
168. C. Marino, E. Marelli and C. Villevieille, *RSC Adv.*, 2017, **7**, 13851-13857.
169. B. Shi, W. Liu, K. Zhu and J. Xie, *Chemical Physics Letters*, 2017, **677**, 70-74.
170. X. Zhu, Q. Li, S. Qiu, X. Liu, L. Xiao, X. Ai, H. Yang and Y. Cao, *Jom*, 2016, **68**, 2579-2584.
171. Y. Liu, F. Fan, J. Wang, Y. Liu, H. Chen, K. L. Jungjohann, Y. Xu, Y. Zhu, D. Bigio, T. Zhu and C. Wang, *Nano Lett.*, 2014, **14**, 3445-3452.
172. L. Seidl, N. Bucher, E. Chu, S. Hartung, S. Martens, O. Schneider and U. Stimming, *Energy Environ. Sci.*, 2017, **10**, 1631-1642.

173. H. Kim, J. Hong, G. Yoon, H. Kim, K.-Y. Park, M.-S. Park, W.-S. Yoon and K. Kang, *Energy Environ. Sci.*, 2015, **8**, 2963-2969.
174. Y. Sun, L. Zhao, H. Pan, X. Lu, L. Gu, Y. S. Hu, H. Li, M. Armand, Y. Ikuhara, L. Chen and X. Huang, *Nat Commun*, 2013, **4**, 1870.
175. J. Wang, C. Eng, Y. C. Chen-Wiegart and J. Wang, *Nat Commun*, 2015, **6**, 7496.
176. C. Villevieille, M. Ebner, J. L. Gomez-Camer, F. Marone, P. Novak and V. Wood, *Adv. Mater.*, 2015, **27**, 1676-+.
177. A. Darwiche, C. Marino, M. T. Sougrati, B. Fraisse, L. Stievano and L. Monconduit, *J. Am. Chem. Soc.*, 2012, **134**, 20805-20811.
178. X. Han, Y. Liu, Z. Jia, Y. C. Chen, J. Wan, N. Weadock, K. J. Gaskell, T. Li and L. Hu, *Nano Lett*, 2014, **14**, 139-147.
179. Z. Li, X. Tan, P. Li, P. Kalisvaart, M. T. Janish, W. M. Mook, E. J. Luber, K. L. Jungjohann, C. B. Carter and D. Mitlin, *Nano Lett*, 2015, **15**, 6339-6348.
180. M. Gu, A. Kushima, Y. Shao, J. G. Zhang, J. Liu, N. D. Browning, J. Li and C. Wang, *Nano Lett*, 2013, **13**, 5203-5211.
181. A. Kohandehghan, K. Cui, M. Kupsta, J. Ding, E. Memarzadeh Lotfabad, W. P. Kalisvaart and D. Mitlin, *Nano Lett*, 2014, **14**, 5873-5882.
182. A. Nie, L.-y. Gan, Y. Cheng, X. Tao, Y. Yuan, S. Sharifi-Asl, K. He, H. Asayesh-Ardakani, V. Vasiraju, J. Lu, F. Mashayek, R. Klie, S. Vaddiraju, U. Schwingenschlögl and R. Shahbazian-Yassar, *Advanced Functional Materials*, 2016, **26**, 543-552.
183. P. Gao, Y.-Y. Zhang, L. Wang, S. Chen, Y. Huang, X. Ma, K. Liu and D. Yu, *Nano Energy*, 2017, **32**, 302-309.
184. H. Liu, F. Cao, H. Zheng, H. Sheng, L. Li, S. Wu, C. Liu and J. Wang, *Chem Commun (Camb)*, 2015, **51**, 10443-10446.
185. X. W. Xia, Q.; Zhu, Q.; Xie, J.; Wang, J.; Zhuang, D.; Zhang, S.; Cao, G.; Zhao, X., *Materials Today Energy*, 2017, **5**.
186. Q. D. Su, G.; Zhang, J.; Zhong, Y.; Xu, B.; Yang, Y.; Neupane, S.; Li, W., *ACS Nano*, 2014, **8**.
187. J. Sottmann, M. Dimichel, H. Fjellvag, L. Malavasi, S. Margadonna, P. Vajeeston, G. Vaughan and D. S. Wragg, *Angew Chem Int Ed Engl*, 2017, DOI: 10.1002/anie.201704271.
188. K. Xiang, W. Xing, D. B. Ravnsbaek, L. Hong, M. Tang, Z. Li, K. M. Wiaderek, O. J. Borkiewicz, K. W. Chapman, P. J. Chupas and Y. M. Chiang, *Nano Lett*, 2017, **17**, 1696-1702.
189. Y. Xie, H. Wang, G. Xu, J. Wang, H. Sheng, Z. Chen, Y. Ren, C.-J. Sun, J. Wen, J. Wang, D. J. Miller, J. Lu, K. Amine and Z.-F. Ma, *Advanced Energy Materials*, 2016, **6**, 1601306.
190. L. Wang, J. Wang, X. Zhang, Y. Ren, P. Zuo, G. Yin and J. Wang, *Nano Energy*, 2017, **34**, 215-223.
191. B. Farbod, K. Cui, W. P. Kalisvaart, M. Kupsta, B. Zahiri, A. Kohandehghan, E. M. Lotfabad, Z. Li, E. J. Luber and D. Mitlin, *ACS Nano*, 2014, **8**.
192. N. Weadock, N. Varongchayakul, J. Wan, S. Lee, J. Seog and L. Hu, *Nano Energy*, 2013, **2**, 713-719.
193. S. D. Lacey, J. Wan, A. von Wald Cresce, S. M. Russell, J. Dai, W. Bao, K. Xu and L. Hu, *Nano Lett*, 2015, **15**, 1018-1024.
194. S. Komaba, W. Murata, T. Ishikawa, N. Yabuuchi, T. Ozeki, T. Nakayama, A. Ogata, K. Gotoh and K. Fujiwara, *Advanced Functional Materials*, 2011, **21**, 3859-3867.
195. P. Hartmann, C. L. Bender, M. Vracar, A. K. Durr, A. Garsuch, J. Janek and P. Adelhelm, *Nat. Mater.*, 2013, **12**, 228-232.
196. L. Lutz, D. A. D. Corte, Y. Chen, D. Batuk, L. R. Johnson, A. Abakumov, L. Yate, E. Azaceta, P. G. Bruce, J.-M. Tarascon and A. Grimaud, *Adv. Energy Mater.*, DOI: 10.1002/aenm.201701581, 1701581-n/a.
197. M. Otoyama, Y. Ito, A. Hayashi and M. Tatsumisago, *J. Power Sources*, 2016, **302**, 419-425.
198. W. Zhang, D. Schroder, T. Arlt, I. Manke, R. Koerver, R. Pinedo, D. A. Weber, J. Sann, W. G. Zeier and J. Janek, *J. Mater. Chem. A*, 2017, **5**, 9929-9936.
199. K. H. Kim, Y. Iriyama, K. Yamamoto, S. Kumazaki, T. Asaka, K. Tanabe, C. A. J. Fisher, T. Hirayama, R. Murugan and Z. Ogumi, *J. Power Sources*, 2011, **196**, 764-767.
200. C.-M. Wang, *Journal of Materials Research*, 2014, **30**, 326-339.
201. K. E. Johnston, M. T. Sougrati, L. Stievano, A. Darwiche, N. Dupré, C. P. Grey and L. Monconduit, *Chemistry of Materials*, 2016, **28**, 4032-4041.
202. Z. Li, J. Ding and D. Mitlin, *Acc Chem Res*, 2015, **48**, 1657-1665.

